Paleoceanography and Paleoclimatology

RESEARCH ARTICLE
10.1029/2019PA003652

Special Section:
Special Collection to Honor the Career of Robert C. Thunell

Quantification of African Monsoon Runoff During Last Interglacial Sapropel S5

Jessica D. Amies[1], Eelco J. Rohling[1,2], Katharine M. Grant[1], Laura Rodríguez-Sanz[1], and Gianluca Marino[1,3]

[1]Research School of Earth Sciences, The Australian National University, Canberra, ACT, Australia, [2]Ocean and Earth Science, University of Southampton, National Oceanography Centre, Southampton, UK, [3]Department of Marine Geosciences and Territorial Planning, University of Vigo, Vigo, Spain

Key Points:
- We present a quantitative time series estimate of North African monsoon intensification for the interval of sapropel S5 deposition
- Sea level and sea surface temperature records used to deconvolve eastern Mediterranean planktic foraminiferal stable oxygen isotope signal
- Preconditioning of the eastern Mediterranean for sapropel deposition suggested by rapid onset of S5 following increase in African runoff

Supporting Information:
- Supporting Information S1

Correspondence to:
J. D. Amies,
jessica.amies@anu.edu.au

Citation:
Amies, J. D., Rohling, E. J., Grant, K. M., Rodríguez-Sanz, L., & Marino, G. (2019). Quantification of African monsoon runoff during last interglacial sapropel S5. *Paleoceanography and Paleoclimatology*, *34*, 1487–1516. https://doi.org/10.1029/2019PA003652

Received 9 MAY 2019
Accepted 2 AUG 2019
Accepted article online 9 AUG 2019
Published online 29 AUG 2019

Abstract Organic-rich sapropel layers punctuate the eastern Mediterranean sedimentary sequence, recording deep-sea anoxic events. The timing of sapropel deposition coincides with precession minima, which are associated with the northward migration of the monsoon rain belt over North Africa. The resultant increase in monsoon precipitation over the Sahara caused an increase in low-$\delta^{18}O$ freshwater runoff into eastern Mediterranean surface waters, which is reflected by negative $\delta^{18}O$ anomalies in the records of planktic foraminiferal calcite. However, despite extensive research on sapropels, the magnitude of monsoon intensification and freshwater runoff, along with its influence on $\delta^{18}O$, remains elusive. Here, we present a quantification of African monsoon freshwater runoff into the eastern Mediterranean for the period of deposition of last interglacial sapropel S5 (~128.3–121.5 ka). Our method uses a box model of the Mediterranean Sea, which represents different water masses, and has been calibrated using $\delta^{18}O$ from planktic foraminiferal species of different depth and seasonal habitats. The model was constrained with existing records of sea level and sea surface temperature then inverted to deconvolve the $\delta^{18}O$ signal of the surface-dwelling foraminiferal species *Globigerinoides ruber* (w) and calculate the freshwater runoff volume. Our calculated African monsoon runoff suggests large increases in freshwater discharge to the eastern Mediterranean (up to ~8.8 times the modern pre-Aswan Nile discharge). Rapid onset of S5 deposition following the estimated increase in runoff strongly suggests a preconditioning of the eastern Mediterranean for sapropel deposition. Our study also provides insight into the stratification and warming of eastern Mediterranean surface waters during the S5 interval.

1. Introduction

Sapropels are dark, organic-rich layers that are common in eastern Mediterranean sediments. The timing of sapropel deposition is associated with precession minima, when Northern Hemisphere summer insolation maxima caused northward migration of the monsoon rain belt over North Africa (e.g., Hilgen, 1991; Lourens et al., 1996; Emeis, Sakamoto, et al., 2000). The resultant increase in precipitation north of the central Saharan watershed at ~21°N fuelled an increase in monsoon-derived, low-$\delta^{18}O$ freshwater runoff into the predominantly eastern Mediterranean basin (Larrasoaña, Roberts, Rohling, et al., 2003; Marino et al., 2009; Rodríguez-Sanz et al., 2017; Rohling et al., 2002). This freshening of eastern Mediterranean surface waters enhanced stratification of the water column and reduced deep water overturning, inhibiting ventilation of bottom waters. This led to oxygen depletion and eventual anoxia at depth, which enabled the preservation of organic matter (e.g., Vergnaud-Grazzini et al., 1977; Rossignol-Strick et al., 1982; Rohling, 1994; Jorissen, 1999; Emeis, Sakamoto, et al., 2000; Larrasoaña, Roberts, Stoner, et al., 2003; Rohling et al., 2015, and references within). In addition, enhanced productivity increased the organic carbon export to bottom waters (e.g., Calvert et al., 1992; de Lange & ten Haven, 1983; Thomson et al., 1999; van Helmond et al., 2015; Weldeab et al., 2003).

The African monsoon freshwater runoff was channeled into the eastern Mediterranean not only via the Nile but also along the wider North African margin via paleoriver systems that were activated during *Green Sahara* periods (Coulthard et al., 2013; Drake et al., 2013; Grant et al., 2017; Larrasoaña et al., 2013; Larrasoaña, Roberts, Stoner, et al., 2003; Marino et al., 2007; Osborne et al., 2008; Rohling et al., 2002; Scrivner et al., 2004). While other potential freshwater sources, including increased outflow of fresher waters from the Black Sea (Lane-Serff et al., 1997; Olausson, 1991) and increased winter precipitation along the

northern borderlands of the eastern Mediterranean (e.g., Kotthoff et al., 2008; Kutzbach et al., 2014; Milner et al., 2012), cannot be discounted, African monsoon-fuelled runoff is generally accepted as the main source of freshwater to the Mediterranean during times of sapropel deposition (e.g., Hennekam et al., 2014; Larrasoaña, Roberts, Stoner, et al., 2003; Lourens et al., 2001; Osborne et al., 2008, 2010; Rohling et al., 2004, 2015; Rossignol-Strick, 1985).

Freshwater from monsoon-type rainfall has especially negative $\delta^{18}O$ values (Beuning et al., 2002; Gasse, 2000; Hoelzmann, 2000; Sonntag et al., 1979). The addition of large volumes of this isotopically light freshwater to Mediterranean surface waters is reflected in low $\delta^{18}O$ anomalies in planktic foraminiferal calcite $\delta^{18}O$ ($\delta^{18}O_{pf}$) of eastern Mediterranean records (e.g., Thunell & Williams, 1983; Tang & Stott, 1993; Emeis, Struck, et al., 2000; Emeis et al., 2003; Rohling et al., 2004). These low $\delta^{18}O_{pf}$ anomalies, or *sapropel imprints*, hold information regarding the source and volume of the freshwater influx to Mediterranean surface waters during sapropel events. However, the sapropel imprint on $\delta^{18}O_{pf}$ has yet to be separated from the background climatic signal, and freshwater runoff from Africa into the eastern Mediterranean during sapropel events remains largely unquantified.

Here we use a box modeling approach to deconvolve $\delta^{18}O_{pf}$ data and provide a quantification of African monsoon runoff for last interglacial sapropel S5 (~128.3–121.5 ka; Grant et al., 2016). S5 is an especially well-developed sapropel that stands out as a strong anomaly in $\delta^{18}O_{pf}$ records (e.g., Cane et al., 2002; Emeis et al., 2003; Rohling et al., 2002, 2004). Moreover, previous Mediterranean studies over this time interval provide important paleoenvironmental information with which to constrain the box model (Marino et al., 2007; Rodríguez-Sanz et al., 2017; Rohling et al., 2004).

2. Approach

Quantification of the sapropel imprint on Mediterranean $\delta^{18}O_{pf}$ is complicated by spatial differences in the freshwater influence throughout the Mediterranean basin during sapropel events. This is reflected in different $\delta^{18}O$ anomalies recorded for the same sapropel event, depending on species and core (location) used. To address this, we use four spatially distributed cores from the eastern Mediterranean (Figure 1 and Table 1) to compile multispecies planktic foraminiferal stable isotope datasets for S5. The six species selected have been shown previously to exhibit stable isotopic signals characteristic of different Mediterranean water masses that extend from surface to intermediate depth (Rohling et al., 2004). Therefore, their $\delta^{18}O$ reflects the isotopic composition and temperature of seawater for different seasons and depths in the water column. *Globigerinoides ruber* (white), *Orbulina universa*, and *Globigerinoides sacculifer* are known to be summer mixed layer (SML) species. However, *G. ruber* (w) has a high tolerance to low salinity and can opportunistically occupy fresher water habitats at the top of the water column during sapropel events (Rohling et al., 2004; Schiebel & Hemleben, 2017). This makes *G. ruber* (w) ideal for identifying sources of freshwater and tracing its circulation in surface waters. *Globigerinella siphonifera* represents the winter mixed layer, which develops when the more thermally stratified summer surface water masses are mixed into a single surface water mass. *Neogloboquadrina pachyderma* (dextral) and *Globorotalia scitula* inhabit intermediate waters, which lie below the surface waters at approximately 150–600 m depth in the eastern Mediterranean (Rohling et al., 2004).

High-resolution stable oxygen and carbon isotope analyses on multiple planktic foraminiferal species over S5 have been previously published for core KS205 (Figure 2;Cane et al., 2002 ; Rohling et al., 2004). To enable comparison with other eastern Mediterranean sites, the present study adds stable isotope data sets for a full suite of the key species over S5 in core LC21 and Ocean Drilling Program (ODP) Site 967 (ODP 967; Figures 1 and 2). The LC21 data set includes previously published *G. ruber* (w) and *N. pachyderma* (d) data (Grant et al., 2012; Marino et al., 2007, 2015). In addition, previously published data for core ODP 971 for *G. ruber* (w), *N. pachyderma* (d), and *G. scitula* over S5 (Cane et al., 2002; Rohling et al., 2004) have been included here to extend the comparison to a fourth site in the basin (Figure 2).

To quantitatively investigate the Mediterranean $\delta^{18}O_{pf}$ signals for sapropel S5, we have adapted and improved the Mediterranean box model introduced by Rohling et al. (2004, 2014) to make it run as a time series through the study interval, constrained by proxy records for sea level and sea-surface temperature (SST) (section 3.6). The model output provides estimates of the expected foraminiferal calcite $\delta^{18}O$ for the

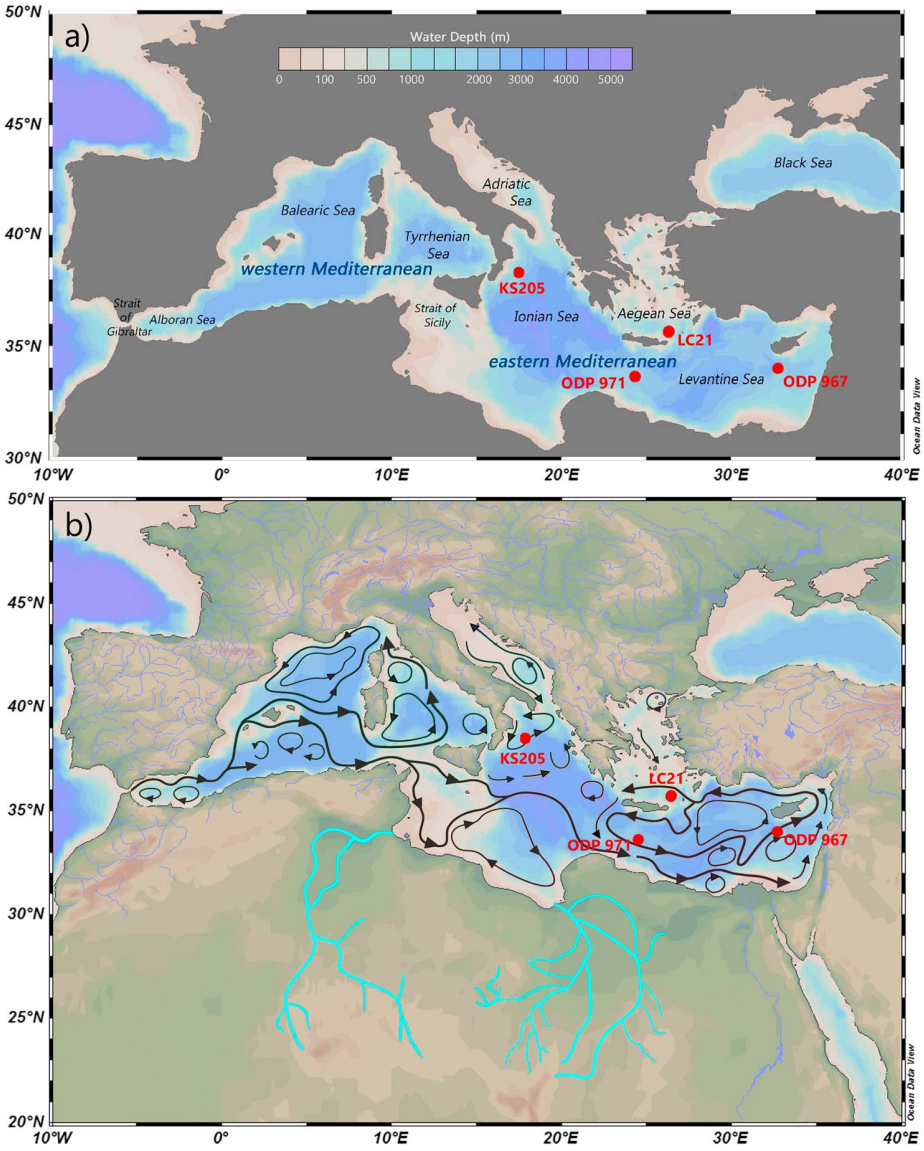

Figure 1. Map of Mediterranean Sea with locations of cores used in study. (a) Mediterranean bathymetry and (b) sea surface circulation schematic (arrows; based on Pinardi et al., 2015, and Rohling et al., 2015), current drainage system (blue), and potential North African paleodrainage networks (cyan; Vörösmarty et al., 2000; Pachur, 2001; Rohling et al., 2002; Osborne et al., 2008; Paillou et al., 2009; Coulthard et al., 2013; Wu et al., 2017). Plot generated with Ocean Data View (Schlitzer, 2016).

different Mediterranean surface and intermediate water masses under a variety of prescribed African monsoon runoff conditions. The multispecies planktic $\delta^{18}O$ data compiled for S5 are compared directly with the model-calculated $\delta^{18}O$ of calcifiers residing in the corresponding Mediterranean water masses.

Table 1
Details of Cores Used in Study (Cane et al., 2002; Shipboard Scientific Party, 1996b, 1996a)

Core	Hole	Latitude	Longitude	Water depth
KS205	-	38°12′N	18°08′E	2,384 m
LC21	-	35°40′N	26°35′E	1,522 m
ODP 967	B	34°04′N	32°43′E	2,554 m
ODP 971	A	33°43′N	24°41′E	2,026 m

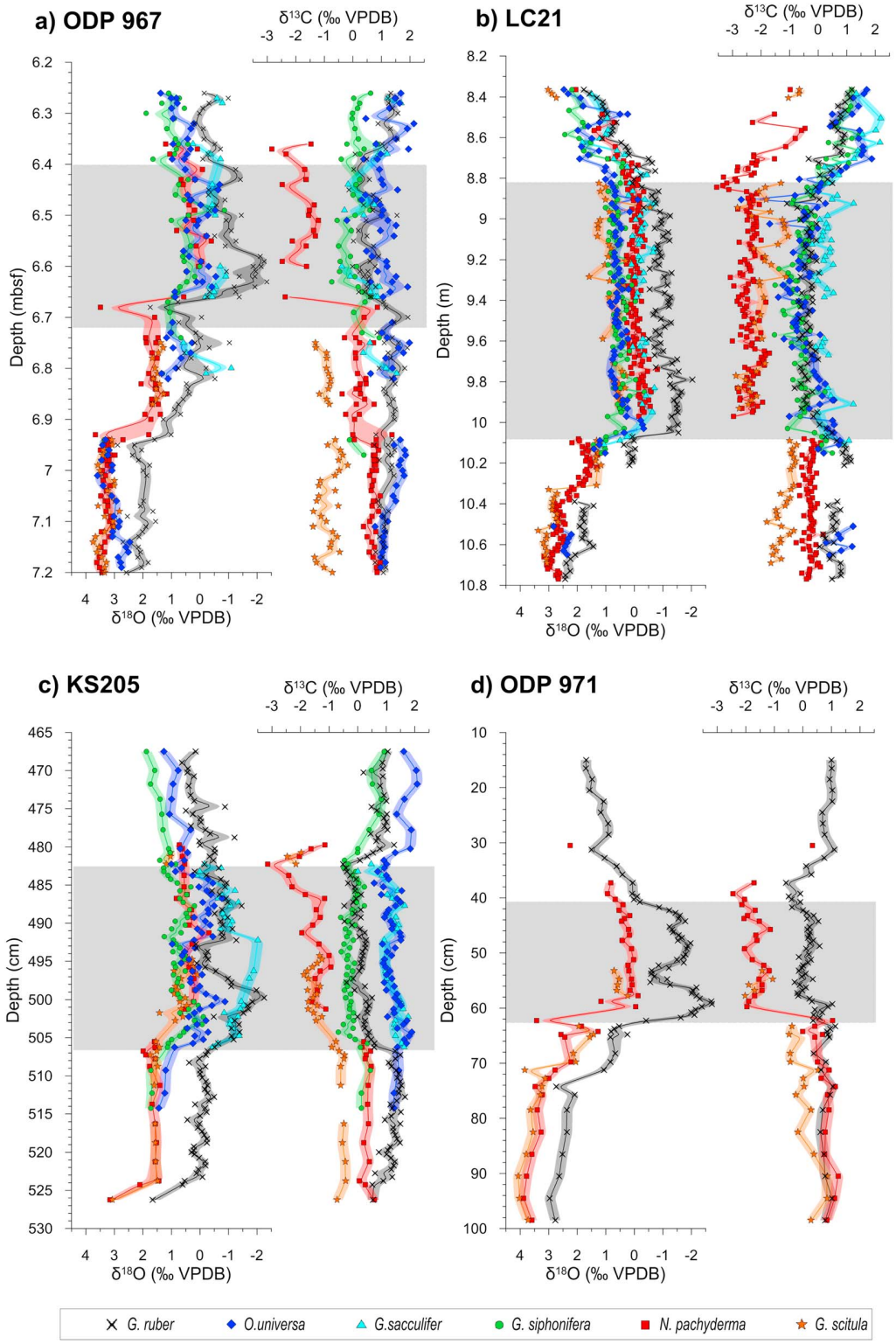

Figure 2. Stable isotope measurements and probabilistic assessments for cores (a) ODP 967, (b) LC21, (c) KS205, and (d) ODP 971. Different species measurements for each core are indicated by colored symbol: *G. ruber* (w; black cross), *O. universa* (dark blue diamond), *G. sacculifer* (light blue triangle), *G. siphonifera* (green circle), *N. pachyderma* (d; red square), and *G. scitula* (orange star). Probability maximum (solid lines), 95% confidence limits (shaded envelopes). Visible extent of the S5 sapropel layer (gray shaded bands). Previously published data are used for KS205 and ODP 971 (Cane et al., 2002; Rohling et al., 2004) and LC21 *G. ruber* (w) and *N. pachyderma* (d; Marino et al., 2007, 2015; Grant et al., 2012).

Using this data-model comparison, a series of experiments is designed to diagnose (a) the best SST proxies to constrain temperature in the model and (b) temporal changes in surface stratification during the study interval.

Following confirmation through data-model comparison that the Mediterranean box model reasonably approximates the Mediterranean system during the S5 study interval, amount and $\delta^{18}O$ of African monsoon freshwater runoff are the only parameters that remain unquantified. This enables us to invert the box model (section 6.1) and use proxy records of sea level and SST for the S5 interval as inputs, along with the $\delta^{18}O$ record for *G. ruber* (w) ($\delta^{18}O_{ruber}$) from the S5 data set. The inverted box model then calculates a time series of the monsoon freshwater volume required to produce the observed eastern Mediterranean $\delta^{18}O_{pf}$ anomaly throughout S5.

3. Materials and Methods

3.1. Marine cores

The four S5 sapropels included in this study are from core sites ODP 967 (eastern Levantine Sea), LC21 (southern Aegean Sea), KS205 (northwestern Ionian Sea), and ODP 971 (central eastern Mediterranean; Table 1 and Figure 1). These sites provide a broad spatial coverage of the eastern Mediterranean for investigating hydrographic changes over a sapropel event. Data for cores KS205 and ODP 971 are presented at 0.5-cm downcore resolution, ODP 967 data at 1-cm resolution, and LC21 data at 1–2-cm resolution.

3.2. Stable Isotopes

For stable isotope analysis, approximately 2 cm^3 of bulk sediment was washed through a 63-μm sieve using reversed osmosis (RO) water. The >63-μm fraction was then oven-dried overnight at 45 °C before being sieved through 150- and 300-μm meshes. *Globigerinoides ruber* (white), *Orbulina universa*, *Globigerinoides sacculifer* (*trilobus* type), and *Globigerinella siphonifera* were picked from the >300-μm fraction, and *Neogloboquadrina pachyderma* (dextral) and *Globorotalia scitula* were picked from the 150–300-μm fraction. All species were picked according to a strict morphology and within a narrow (35–50 μm) size range (*G. ruber* [w] and *O. universa*, 325–375 μm; *G. sacculifer*, 375–425 μm; *G. siphonifera*, 475–525 μm; *N. pachyderma* (d), 200–235 μm; and *G. scitula*, 235–270 μm). Prior to analysis, foraminiferal tests were crushed and then cleaned by brief ultrasonication in methanol. Stable isotope measurements were performed using a Thermo Scientific DELTA V Isotope Ratio Mass Spectrometer coupled with a KIEL IV Carbonate Device. Results are reported in per mil deviations from Vienna PeeDee Belemnite using NBS-19 ($\delta^{18}O = -2.20‰$, $\delta^{13}C = 1.95‰$) and NBS-18 ($\delta^{18}O = -23.20‰$, $\delta^{13}C = -5.014‰$) carbonate standards. An internal standard (ANU-M2) was run alongside the samples and yielded average values of $\delta^{18}O = -7.40 \pm 0.09‰$ (1σ) and $\delta^{13}C = 2.83 \pm 0.04‰$ (1σ).

3.3. Probabilistic Assessments

Probabilistic assessments of uncertainties in depth and $\delta^{18}O$ or $\delta^{13}C$ were performed for the stable isotope data sets of all four cores. Confidence levels for $\delta^{18}O$ and $\delta^{13}C$ signals of different species were calculated taking into account uncertainties for isotopic measurements (analytic and natural variability, 1σ uncertainty range ± 0.1‰) and downcore depths (3σ uncertainty range equals sampling resolution for individual cores, i.e., ±0.25 cm for KS205 and ODP 971, ±0.5 cm for ODP 967, and ±1 cm for LC21). Individual data points were randomly sampled 10,000 times within their uncertainties in Monte Carlo-style simulations using MATLAB, following previous studies (e.g., Grant et al., 2012; Marino et al., 2015; Rohling et al., 2014; Thirumalai et al., 2016). The probability maximum was calculated from the modal value of the 10,000 Monte Carlo simulations at each depth step. Percentiles taken from the distribution of the simulations at each depth step enabled determination of the 68% (16th to 84th percentile) and 95% (2.5th to 97.5th percentile) probability intervals. All results were then interpolated and smoothed to suppress noise and short-term variability using a Gaussian filter with defined depth windows: 0.25 cm for KS205 and ODP 971 and 0.5 cm for ODP 967 and LC21 (i.e., half of the maximum sampling resolution).

3.4. Stratigraphic Correlation

All S5 intervals were aligned on a common depth scale, based on Cane et al.'s (2002) stratigraphic correlation framework for the same cores. Cane et al. (2002) placed KS205 on an ODP 971A-equivalent depth using

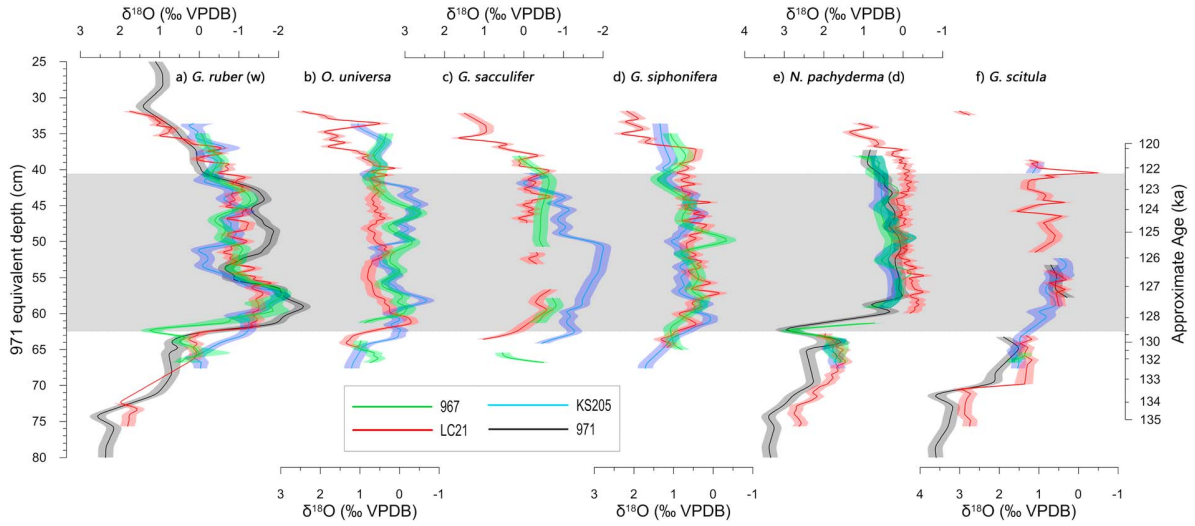

Figure 3. Probabilistic assessments of stable oxygen isotope measurements for species (a) *G. ruber* (w), (b) *O. universa*, (c) *G. sacculifer*, (d) *G. siphonifera*, (e) *N. pachyderma* (d), and (f) *G. scitula* on ODP 971A-equivalent depth scale. Data from different cores are indicated by color: ODP 967 (green), LC21 (red), KS205 (blue), and ODP 971 (black). Probability maximum (solid lines), 95% confidence limits (shaded envelopes). Visible extent of the S5 sapropel layer in ODP 971 (grey shaded band).

distinct events in planktic foraminiferal abundance and isotope observations as correlation markers and then fitting both linear and polynomial fits through the markers. The polynomial fit was then used to map the core onto the ODP 971A depth scale. The method has since been applied to S5 in LC21 (Marino et al., 2007) and is here applied to S5 in ODP 967B (Supporting Information Table S1 and Figure S1).

The precision of the depth assignments for the correlation markers in ODP 967B was restricted by its sample spacing of 1 cm. A hiatus, identified in ODP 967C by Cane et al. (2002), was not discernible in our investigation of ODP 967B. We fitted the correlation markers for ODP 971A and ODP 967B with linear ($y = 0.0134x + 5.8356$ with $N = 14$ and $R^2 = 0.95$, RMSE = 0.025) and polynomial fits ($y = 0.0922 \times 10^3x^2 + 0.0038x + 6.0805$ with $N = 14$ and $R^2 = 0.95$, RMSE = 0.024). However, one primary correlation marker (faunal marker f7, Table S1) had a deviation of ~5 cm from both the linear and polynomial regressions (Figure S1). Excluding this marker significantly improved both the linear ($y = 0.0132x + 5.8449$ with $N = 13$ and $R^2 = 0.97$, RMSE = 0.021) and polynomial fits ($y = 0.1257 \times 10^3x^2 + 0.0147 \times 10^3x + 6.1796$ with $N = 13$ and $R^2 = 0.97$, RMSE = 0.019). Hence, this correlation marker was discarded as an outlier. While the polynomial fit is not statistically better, it has a lower RMSE and provides a better visual fit, and so was used to map ODP 967B onto the ODP 971A depth scale.

The Cane et al. (2002) stratigraphic model relies on markers that are all based closely around the main S5 interval (primary markers are between 39.25 and 65.25 cm on ODP 971A depth; Table S1 and Figure S1). Extending the multisite correlation in an unconstrained manner to sections outside of the stratigraphic model would be unreliable because it would not account for potential changes in sediment accumulation rates, which have been observed for eastern Mediterranean cores (Larrasoaña, Roberts, Stoner, et al., 2003; Revel et al., 2010). Hence, the ODP 967, LC21, and KS205 data sets presented on this depth scale do not have the full extents of their presapropel records included. Regardless, the ODP 971A-equivalent depth scale provides a good intersite comparison of the actual S5 signals (Figure 3).

3.5. Age Model

The ODP 971A-equivalent depth scale does not have an associated age model. However, an age model has been developed for core LC21 using correlation of LC21 *G. ruber* $\delta^{18}O$ to the U-Th dated Soreq Cave speleothem $\delta^{18}O$ record (Bar-Matthews et al., 2000; Grant et al., 2012). Using the stratigraphic correlation between cores ODP 971A and LC21 (Cane et al., 2002; Marino et al., 2007), the ODP 971A depth scale can be transferred to the LC21 age model.

3.6. Mediterranean Box Model

3.6.1. Model Adaptation

The Mediterranean box model used here is an adapted version (in MATLAB) of the Rohling et al. (2014) model, which in turn drew on that of Rohling et al. (2004). The latter was a seasonally separated version of an earlier box model of the Mediterranean (Rohling, 1999) coupled to a model of exchange transport with the Atlantic at the Strait of Gibraltar (Bryden & Kinder, 1991). The model was further developed by Rohling et al. (2014), but unquantified monsoon influences during sapropel events caused those authors to exclude these intervals (and the model's *monsoon box*) from their study. For our study, the monsoon box of Rohling et al. (2004) was reinstated. The monsoon box allows excess monsoon freshwater associated with sapropel events to be input into the surface waters of the model during a 2-month *monsoon season*. This implies that during times of increased freshwater influx, the SML stratifies into a fresher *upper summer mixed layer* (USML) and a *lower summer mixed layer* (LSML) underlying it. This allows for the fresher, more buoyant waters to remain, more realistically, at the top of the water column during the monsoon season, instead of being immediately mixed throughout the full depth of the SML. The USML effectively represents the uppermost layer that is affected by freshwater input into the basin in the form of freshwater layers or lenses (Rohling et al., 2004). The depth of this freshwater-diluted USML is unknown, but approximations are explored in diagnostic experiments (section 5.2).

The model also required further development to run in a continuous mode throughout the S5 time interval. We ran the model for a series of progressive 25 year step intervals from 134.6 to 116.7 ka, with the model iterating 25 times at each step to correspond to the number of annual cycles represented. The 25-year interval is substantially longer than the residence time for the surface mixed layer during sapropel events (~11 years, as calculated by the model). Hence, we assume that for each age step at which the model is run, the different water masses in the basin reach a steady state.

3.6.2. Inputs

The Red Sea sea level record of Grant et al. (2012) was used to force sea level in the box model, as it is a continuous, highly resolved and independently dated (i.e., radiometrically assessed) record that is closely correlated to the Mediterranean records (Grant et al., 2012) and that covers sapropel S5.

Eastern Mediterranean SST records based on both the alkenone unsaturation index ($U^{K'}_{37}$; Rohling et al., 2002; Marino et al., 2007) and carbonate clumped isotope thermometry (Δ_{47}) for *G. ruber* (w; Rodríguez-Sanz et al., 2017) are used as inputs for the Mediterranean box model in this study (see section 5.1). $U^{K'}_{37}$-based SST reconstructions exist for the S5 interval at all four of the eastern Mediterranean sites included in this study (Marino et al., 2007; Rohling et al., 2002, 2004). Each SST record was transferred onto the ODP 971A-equivalent depth scale as described in section 3.4. An eastern Mediterranean $U^{K'}_{37}$-based SST stack of the four records was created using a Monte Carlo simulation, which was run 10,000 times, each time sampling the data points from all four cores from within their 3σ uncertainty ranges (Figure 4a). The resultant outputs from the simulation were used to calculate the 2.5th, 16th, 50th, 84th, and 97.5th percentiles of the probability distribution. From this we obtained the median, along with 68% (16th to 84th percentile) and 95% (2.5th to 97.5th percentile) probability envelopes of the stack, which were then mapped onto the LC21 age scale (section 3.5), and smoothed using a Gaussian filter with a 2-kyr window, which is the age uncertainty of the age model for this interval (Grant et al., 2012). Δ_{47}-based SST records have been constructed using *G. ruber* (w) for sites LC21 and ODP 967 over the S5 time interval (Rodríguez-Sanz et al., 2017). The Δ_{47}-based SST eastern Mediterranean stack has been created from the two records using the *nontraditional data analysis* method described in Rodríguez-Sanz et al. (2017). This follows the same philosophy as described above for the $U^{K'}_{37}$-based SST stack but incorporates Δ_{47} to temperature conversion and transfer onto the age model in the Monte Carlo simulations, before smoothing using a 5-kyr Gaussian filter (Figure 4b).

3.6.3. Uncertainty Propagation Through the Model

Each input variable and prescribed parameter within the model has an associated uncertainty or range of possible values (Table S2). These are defined in the model as probability distribution functions. To fully account for these uncertainties, they need to be propagated through the model. This was done using a Monte Carlo-style approach in which the model is run 10,000 times, each time sampling the different parameters from within their uncertainties. The resultant 10,000 model outputs from all the model runs were then used to calculate the 2.5th, 16th, 50th, 84th, and 97.5th percentiles of the probability distributions for

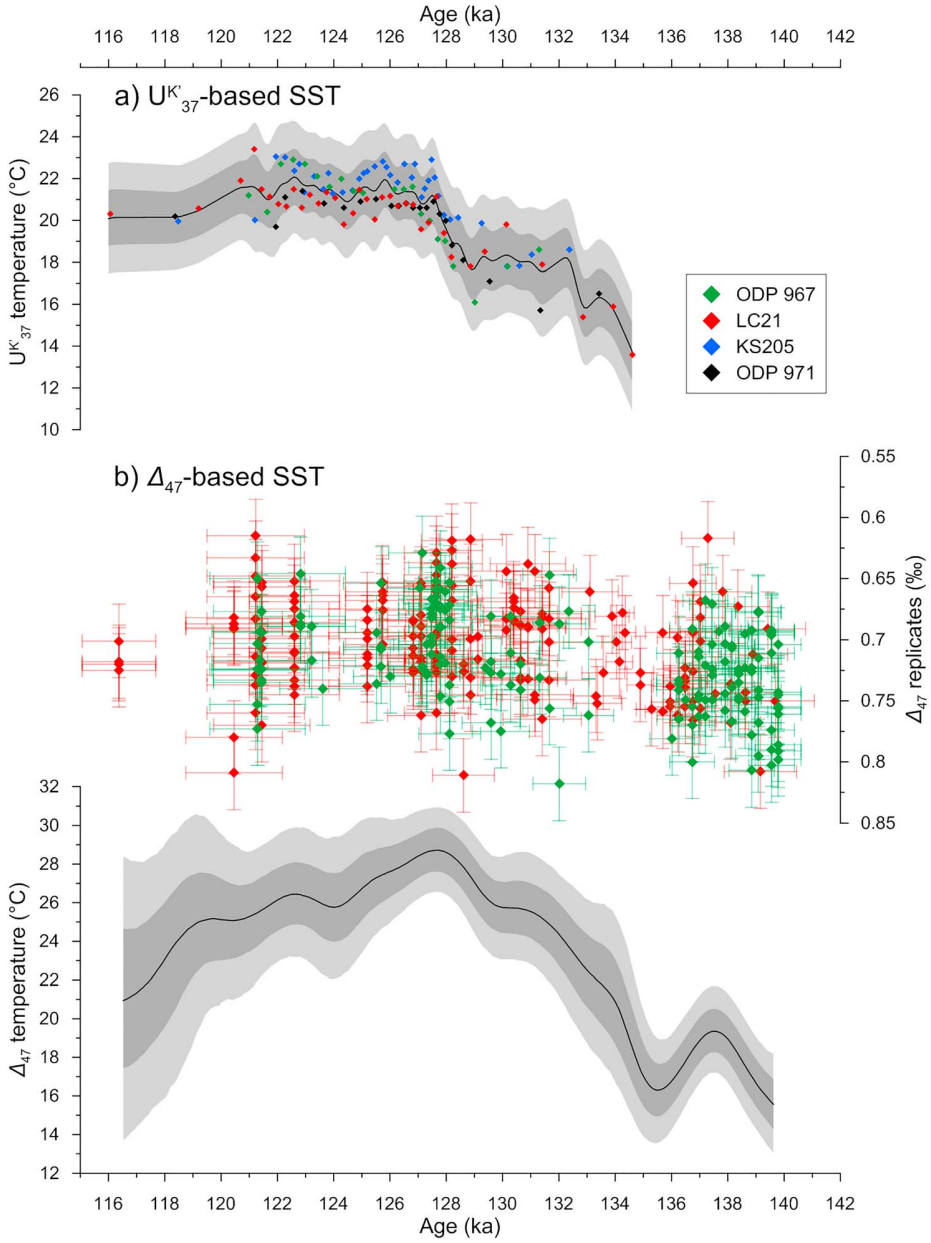

Figure 4. Eastern Mediterranean temperature stacks for (a) $U^{K'}_{37}$ and (b) Δ_{47}-*G. ruber* (w) paleothermometers. Medians (solid lines), 68% and 95% confidence limits (shaded envelopes). Individual data points from different cores are indicated by color: ODP 967 (green), LC21 (red), KS205 (blue), and ODP 971 (black). Records have been transferred onto LC21 age model via ODP 971A-equivalent depth scale, to which LC21 is stratigraphically correlated.

each output parameter. This allowed the median and 68% (16th to 84th percentile) and 95% (2.5th to 97.5th percentile) probability envelopes of all the calculated output parameters to be defined.

4. Stable Isotope Results

Below the visible S5 interval in each core, there is a simultaneous $\delta^{18}O$ decrease of 1‰ or more in all species where present (at 6.94 mbsf in ODP 967, 10.35 m in LC21, 525 cm in KS205, and 73 cm in ODP 971; Figure 2). *G. sacculifer* and *G. siphonifera* were not observed in any of the study cores until just below the S5 layer. Within S5, all species included in this study display shifts to more negative $\delta^{18}O$ (Figure 3), albeit to different

extents. Minimum amplitude change is ~1‰ in *G. scitula*, and maximum change is greater than 3‰ in ODP 971 *G. ruber* (w). Abrupt $\delta^{18}O$ decreases mark the start of S5, while more gradual $\delta^{18}O$ increases occur at the end of the sapropel. Shifts to lower $\delta^{13}C$ during S5 are also evident across all records, with amplitude changes varying greatly between species, from ~0.5‰ in *O. universa* and *G. sacculifer*, up to ~2.5‰ in *N. pachyderma* (d; Figure 2).

Of all the species in our study, $\delta^{18}O_{ruber}$ displays the greatest negative excursions and also the greatest spatial and temporal variability (Figure 3). For each core, the $\delta^{18}O_{ruber}$ anomaly is most pronounced at the start of S5, from the base of the sapropel layer at 62.5 cm up to approximately 55 cm on the ODP 971A-equivalent depth scale; this clearly defined interval of S5 is referred to as the *lower lobe* (Rohling et al., 2004). ODP 971A has the most negative $\delta^{18}O_{ruber}$ signal over the lower lobe, reaching −2.5‰ at 59 cm. ODP 967 and KS205 display similar amplitude excursions, both reaching approximately −2‰ at 52 cm, while LC21 shows the smallest amplitude change in $\delta^{18}O_{ruber}$. ODP 971A and KS205 display a very clear positive excursion in $\delta^{18}O_{ruber}$ above the lower lobe (i.e., an *interruption* in the freshwater signal), before returning to a more negative $\delta^{18}O_{ruber}$ for the *upper lobe* from ~51 cm up to 41 cm (although not as negative as within the lower lobe).

The interruption in the S5 $\delta^{18}O_{ruber}$ signal has been reported by several previous studies (e.g., Rohling et al., 2002, 2004; Scrivner et al., 2004). The duration of the interruption is longer in KS205 (~56 to 50 cm on the ODP 971A-equivalent depth scale) than in ODP 971 (~56 to 52 cm). ODP 967 and LC21 do not show an interruption but instead display an increase in $\delta^{18}O_{ruber}$ above the lower lobe to approximately −1‰, which is maintained for the remainder of the sapropel interval. Similar to the lower lobe, ODP 971 also reaches the most negative $\delta^{18}O_{ruber}$ of all cores in the upper lobe. There are some fluctuations in the signals, but over the upper lobe ODP 967, LC21, and KS205 have comparable $\delta^{18}O_{ruber}$.

No records exist for *O. universa*, *G. sacculifer*, and *G. siphonifera* over S5 for core ODP 971, and no samples were available to generate them for this study. In the other three cores, signals for *O. universa*, *G. sacculifer*, and *G. siphonifera* are harder to compare than other species because these species are not continuously present throughout the entire study interval, in particular prior to the start of S5 (Figure 3). The lack of a pre-sapropel record makes it difficult to discern amplitude changes for these species. Despite this, there are *O. universa*, *G. sacculifer*, and *G. siphonifera* records for the sapropel itself. While *O. universa* $\delta^{18}O$ signals ($\delta^{18}O_{universa}$) appear to closely covary in ODP 967 and KS205, they show heavier values in LC21, with different variability throughout the sapropel. KS205 $\delta^{18}O_{universa}$ shows evidence of the freshwater signal interruption that was also observed in $\delta^{18}O_{ruber}$. *G. sacculifer* records across S5 are discontinuous and highly variable between cores. Notably, $\delta^{18}O_{sacculifer}$ reaches values as low as −2‰ within S5 in KS205, where it is the only $\delta^{18}O$ signal to exceed −1‰ other than that of *G. ruber*. In ODP 967 and LC21, $\delta^{18}O_{sacculifer}$ remains around −0.5‰. *G. siphonifera* $\delta^{18}O$ values ($\delta^{18}O_{siphonifera}$) are relatively similar in all three cores, with the signals over S5 largely remaining between 0 and 1‰ during S5.

N. pachyderma (d) $\delta^{18}O$ records ($\delta^{18}O_{pachyderma}$) for ODP 967, KS205, and ODP 971 are virtually indistinguishable during S5 within errors, and LC21 $\delta^{18}O_{pachyderma}$ is only slightly lower (by less than 1‰), particularly at the beginning and end of S5 (Figure 3). *N. pachyderma* (d) shows the least $\delta^{18}O$ variability within S5 of all species in this study. Amplitude changes in $\delta^{13}C$ are greatest for *N. pachyderma* (d) of all species, with a very rapid decrease in $\delta^{13}C_{pachyderma}$ at the start of S5 (Figure 2). There is also a distinct negative $\delta^{13}C_{pachyderma}$ peak at the end of S5 in all cores.

G. scitula is mostly absent during S5, with the exception of core LC21, but, where present, it shows good coherence in $\delta^{18}O$ between sites (Figure 3). *G. scitula* $\delta^{18}O$ values ($\delta^{18}O_{scitula}$) closely follow those of *N. pachyderma* before S5. However, $\delta^{18}O_{scitula}$ has a smaller amplitude of change than $\delta^{18}O_{pachyderma}$ associated with S5. A smaller amplitude of change is also observed in $\delta^{13}C_{scitula}$ compared with $\delta^{13}C_{pachyderma}$ (Figure 2).

5. Box Model Diagnostic Experiments

The following Mediterranean box model experiments are designed to investigate and refine our constraint of two key parameters in the model: (a) SST (section 5.1) and (b) thickness of the USML (section 5.2).

Both ice volume/sea level and temperature proxies are used as inputs to constrain the Mediterranean model (Figure 5). To constrain sea level we use the record of Grant et al. (2012) as it is highly resolved over our study

interval and is validated within the uncertainties of several other reconstructions (e.g., Elderfield et al., 2012; Hibbert et al., 2016; Kopp et al., 2009; Rohling et al., 2008). Temperature, on the other hand, is more difficult to constrain because it is site, season, and depth specific, hence the SST diagnostics (section 5.1).

The study interval for all diagnostics includes times before and after sapropel S5, when there is no evidence of excess freshwater input from an enhanced African monsoon. In addition, there is an interruption interval within S5, where excess freshwater influx is thought to have diminished, if not completely ceased (Cane et al., 2002; Rohling et al., 2002, 2004; Scrivner et al., 2004). To model both *sapropel-forming* conditions and *normal* conditions, different stages were defined within the study interval (Table 2). These stages were identified by the visible sapropel layers in the sediment cores and features observed in the $\delta^{18}O$ data set (section 4). The different stages were set to have the excess monsoon freshwater input switched to either an *on* or *off* mode, similar to the approach of Rohling et al. (2004). In the on mode, excess freshwater runoff is input into the surface USML box during the 2-month monsoon season. In the off mode, excess freshwater runoff input is set to 0, and the SML remains as one homogeneous layer throughout the six-month summer season.

The as-yet unquantified parameters of volume and $\delta^{18}O$ of the excess monsoon freshwater runoff to the Mediterranean during the sapropel intervals are set to account for a range of possible values. Rohling et al. (2004) provided estimates of the volume of monsoon freshwater runoff for S5, suggesting increases in total runoff of 160–300% during the earlier (*lower*) lobe of S5 and of 120–200% during the later (*upper*) lobe. Therefore, in these experiments, excess freshwater runoff volume is defined as a factor increase of the normal present-day (pre-Aswan damming) total runoff input volume (0.45×10^{12} m^3/year; Carter, 1956; Schink, 1967; Garrett et al., 1993). In addition, several studies (Al Faitouri & Sanford, 2015; Beuning et al., 2002; Hoelzmann, 2000; McKenzie, 1993; Rodrigues et al., 2000; Thorweihe et al., 1990) indicate that the monsoon freshwater that affected regions of North Africa that are today covered by the Saharan desert was isotopically very light, with $\delta^{18}O$ between ~ −8‰ and −12‰. These estimates are used as initial constraints to monsoon runoff volume and its $\delta^{18}O$. The model accounts for the ranges of estimates in the same way that uncertainties are accounted for with other input parameters. The monsoon parameters are defined as a median value with a 3 standard deviation range corresponding to the known range of possible values for the parameter in question (see Table 2).

5.1. SST Diagnostics

Here, we use temperature records from the two different proxies available across S5; the clumped isotopes (Δ_{47}) and alkenone ($U^{K'}_{37}$) paleothermometers, which we compile into eastern Mediterranean stacks to provide representative temperature approximations for the basin-mean state (Figure 4; section 3.6; Rohling et al., 2002, 2004; Marino et al., 2007; Rodríguez-Sanz et al., 2017). The Δ_{47}-based SST reconstruction is measured on *G. ruber* (w) and hence is a specific record of temperature for *G. ruber* (w)'s habitat, that is, the SML, or freshwater lenses/USML during the monsoon season (Emeis et al., 2003; Rodríguez-Sanz et al., 2017; Rohling et al., 2004). Previously, the Rohling et al. (2004) model used $U^{K'}_{37}$-based SST as representative of annual mean SST, with a superimposed seasonal deviation of ±3 °C applied for summer/winter (after Stanev et al., 1989). While this seasonal deviation is based on modern observations, we maintain this seasonality in our study as Mediterranean SST paleoseasonality is not well understood and remains unconstrained for the study interval. However, $U^{K'}_{37}$-based reconstructions represent temperatures during the season of maximum haptophyte production, which in the eastern Mediterranean is typically observed during winter and spring (Castañeda et al., 2010; Goudeau et al., 2014; Leider et al., 2010). Therefore, the $U^{K'}_{37}$-based SST reconstructions are biased toward winter SSTs, although the extent of this is not well quantified. As the *G. ruber*-Δ_{47} temperature reconstruction should reflect SML SST, the seasonal offset we apply to $U^{K'}_{37}$ to represent summer SST should not exceed that of Δ_{47}-based SST. $U^{K'}_{37}$-based SST + 5 °C is greater than Δ_{47}-based SST from 124.35 ka onward, indicating that a summer offset of 5 °C is too large. $U^{K'}_{37}$-based SST + 4 °C is greater than Δ_{47}-based SST for a short interval from 118.65 to 116.7 ka, but both SST records over this interval are constructed from relatively few data points and have large uncertainties (Figure 4). Therefore, to both satisfy this constraint and reflect the winter bias of $U^{K'}_{37}$, we suggest a summer/winter deviation of around +4/−2 °C is most appropriate for the $U^{K'}_{37}$-based SST. The different information provided by both the Δ_{47} and $U^{K'}_{37}$ SST proxies is exploited to test seasonal SST constraints in our model.

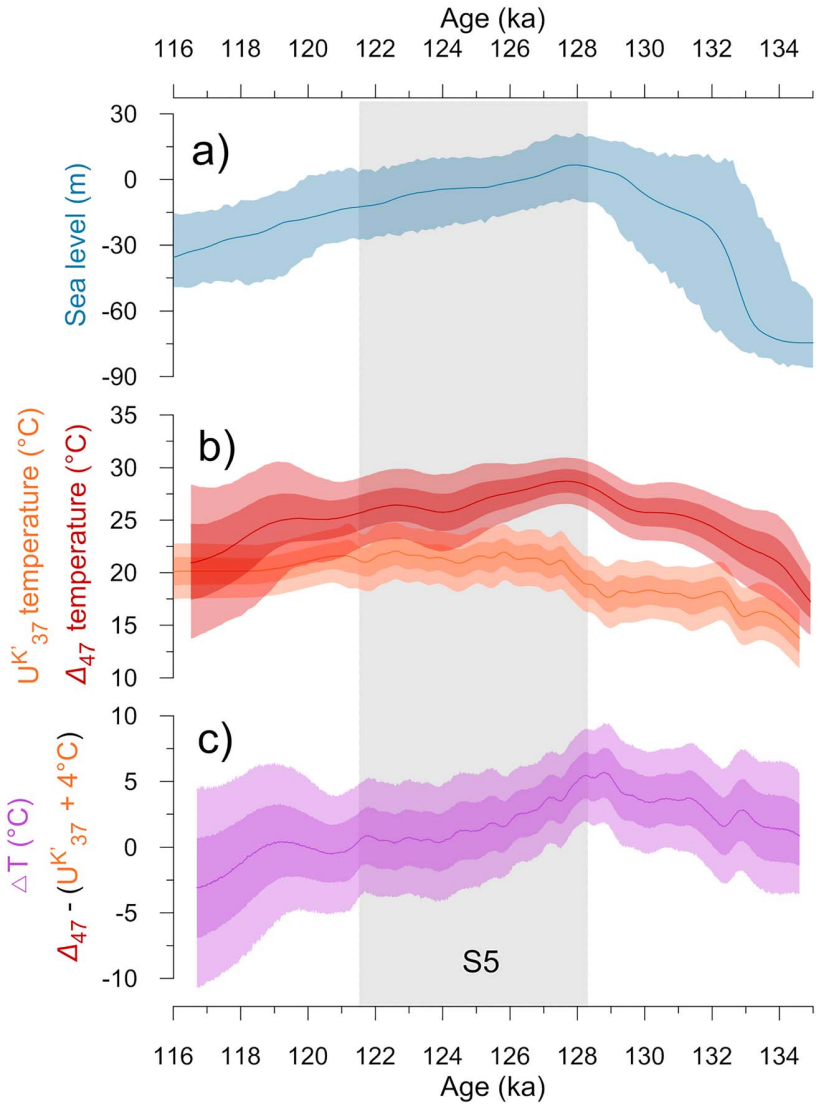

Figure 5. Proxy inputs for Mediterranean box model: (a) Red Sea sea level record (Grant et al., 2012), (b) eastern Mediterranean stacks for $U^{K'}_{37}$-based SST (orange; original data from Rohling et al., 2002, 2004; Marino et al., 2007) and *G. ruber* (w) Δ_{47}-based SST record (red; original data from Rodríguez-Sanz et al., 2017), (c) difference between the Δ_{47}-based and $U^{K'}_{37}$-based (+4 °C summer deviation) SST records (ΔT). Medians (solid lines), 68% and 95% confidence limits (shaded envelopes). S5 interval (gray shaded band).

Table 2
Different Stages in the Study Interval and Associated Monsoonal Parameters as set in the Mediterranean Box Model for Diagnostic Experiments

Interval	Age (ka)	Excess monsoonal freshwater input On/off	Monsoonal runoff parameters	
			Volume	$\delta^{18}O$
Presapropel	>128.6	Off	0	N/a
S5 lower lobe	128.6–126.9	On	*1.6–3.0 x total present-day runoff*	−8 to −12‰
Freshwater runoff interruption	126.9–125.8	Off	0	N/a
S5 upper lobe	125.8–122.5	On	*1.2–2.0 x total present-day runoff*	−8 to −12‰
Postsapropel	<122.5	Off	0	N/a

Table 3
Constraints for Diagnostic Experiments

SST diagnostic experiments		
Experiment	**SST constraint**	**Depth of USML (m)**
SST_A	6-month summer: $U^{K'}_{37}$-based SST record (+4 °C summer deviation) 6-month winter: $U^{K'}_{37}$-based SST record (−2 °C winter deviation)	5 m
SST_B	6-month summer: Δ_{47}-based SST record 6-month winter: $U^{K'}_{37}$-based SST record (−2 °C winter deviation)	5 m
SST_C	4-month summer: $U^{K'}_{37}$-based SST record (+4 °C summer deviation) 2-month monsoon season: Δ_{47}-based SST record 6-month winter: $U^{K'}_{37}$-based SST record (−2 °C winter deviation)	5 m

Depth of USML diagnostic experiments

Experiment	**Summer SST constraint**	**Minimum depth of USML (m) ΔT = 6.79 °C**	**Maximum depth of USML (m) $\Delta T \leq 0$ °C**	**Equation**
zUSML_A	*As for SST_C*	1.5	30	zUSML = −5.000 ΔT + 30
zUSML_B	*As for SST_C*	5	30	zUSML = −4.386 ΔT + 30
zUSML_C	*As for SST_C*	10	30	zUSML = −3.509 ΔT + 30

5.1.1. Experimental Setup

To test which SST records are best for constraining summer SST in the model, we run the model with three different summer SST scenarios, while all other inputs are kept constant (experiments SST_A, SST_B, and SST_C; Table 3). Experiments SST_A and SST_B constrain summer temperatures using the $U^{K'}_{37}$-based SST record and Δ_{47}-based SST records, respectively. Experiment SST_C explores the scenario that the Δ_{47}-based SST record is not representative of the temperature of the entire SML but was instead specifically recording temperatures in the freshwater-stratified USML, where *G. ruber* (w) is thought to have preferentially resided during sapropel events (Emeis et al., 2003; Rohling et al., 2004). It has been proposed that this layer is susceptible to a *temperature concentration* effect, where solar insolation excessively warms thin, isolated surface layers (Emeis et al., 2003). This inference is supported by the difference between the Δ_{47}-*G. ruber* (w) and the $U^{K'}_{37}$-based SST reconstructions (Figure 5; Rodríguez-Sanz et al., 2017). Hence, experiment SST_C constrains 4 months of normal summer using the $U^{K'}_{37}$-based SST record and the summer's last 2-month monsoon season using the Δ_{47}-based SST record (Table 3). As the Δ_{47}-based and $U^{K'}_{37}$-based (with +4 °C summer deviation) SST records are different even outside of S5 (Figure 5), it is implicitly assumed in this experiment that *G. ruber* (w)'s depth habitat may have been skewed toward shallower depths in the SML at all times, not only when there are less saline surface waters during enhanced monsoon runoff events. To reflect this in the model, for SST_C the USML is considered throughout the study interval, not only during S5. However, during normal times (outside of S5), the USML receives only its normal share of annual runoff, as opposed to receiving additional *excess runoff*, which during the sapropel interval accounts for increased monsoon freshwater input to the basin. In doing this, the USML represents a shallower depth habitat of *G. ruber* (w) within the SML. The other SML dwellers (*O. universa* and *G. sacculifer*) are assumed to be continuously homogeneously distributed throughout the depth of the entire SML. For the SST diagnostic experiments, the depth of the USML is set to a basin-mean value of 5 m, following Rohling et al. (2004).

5.1.2. Results

To identify the best SST scenario, the SST diagnostic model results for expected foraminiferal $\delta^{18}O$ of the freshwater-diluted USML and the main body of the SML are compared with the actual $\delta^{18}O$ data for *G. ruber* (w), *O. universa*, and *G. sacculifer*. To approximate basin-mean records for these species, the S5 $\delta^{18}O$ records from cores ODP 967, LC21, KS205, and ODP 971 (Figure 3) were first stacked using a Monte Carlo-style probabilistic assessment (Figure 6; method as described for the $U^{K'}_{37}$-based SST stack, section 3.6).

We first consider experiment SST_A (Figure 7a). $\delta^{18}O$ outputs from the model are much heavier than the data, particularly during S5 from 128.3 to 123 ka. The $\delta^{18}O_{universa}$ and $\delta^{18}O_{sacculifer}$ records are at the edge of the 95% bounds, which represents the most extreme monsoon runoff parameters considered, and the amplitude change in observed $\delta^{18}O_{ruber}$ during S5 is far greater than the model output envelope, by more

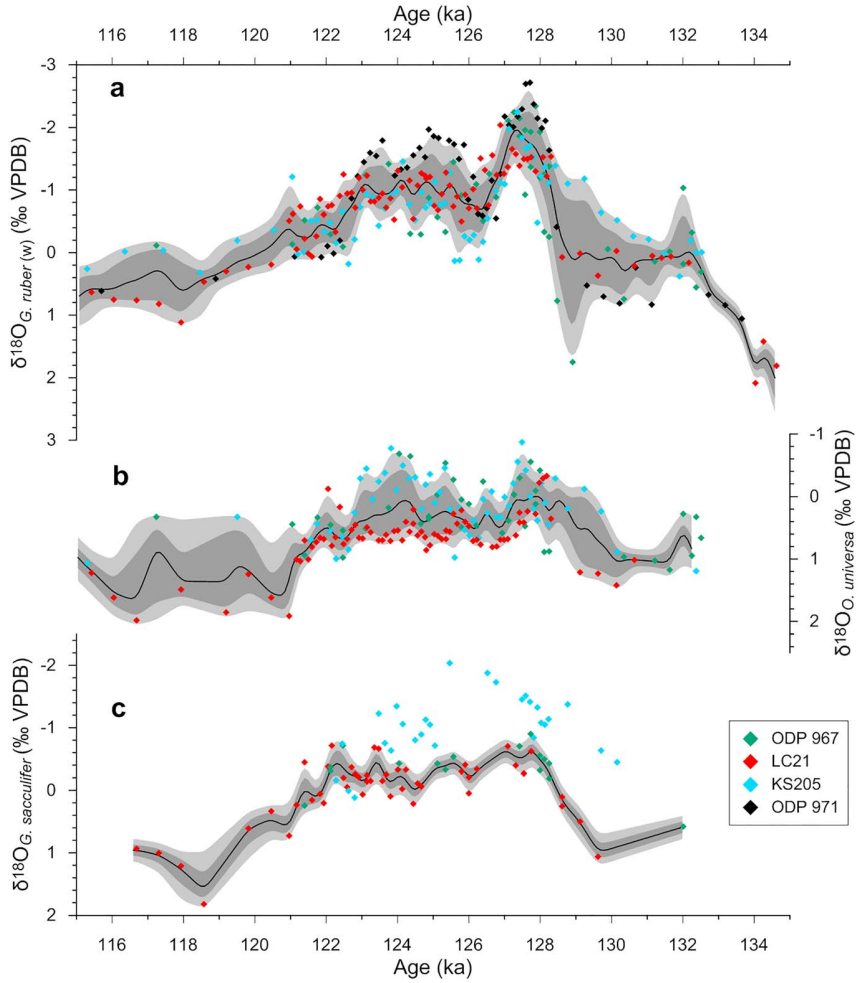

Figure 6. Eastern Mediterranean $\delta^{18}O$ stacks for (a) *G. ruber* (w), (b) *O. universa*, and (c) *G. sacculifer*. Medians (solid lines), 68% and 95% confidence limits (shaded envelopes). Individual data points from different cores are indicated by color: ODP 967 (green), LC21 (red), KS205 (blue), and ODP 971 (black). Note that the *G. sacculifer* $\delta^{18}O$ stack was calculated from records for ODP 967 and LC21 only because KS205 results were anomalous for this species. Records have been transferred onto LC21 age model via ODP 971A-equivalent depth scale, to which LC21 is stratigraphically correlated.

than 1‰ in the lower lobe of S5. Not much difference exists between the modeled $\delta^{18}O$ for the freshwater-diluted USML and the main body of the SML, especially in the upper lobe of S5 where they cannot be differentiated. Thus, experiment SST_A suggests that use of only the $U^{K'}37$-based SST record (+4 °C) is inconsistent with the $\delta^{18}O$ observations in summer species and that it underestimates SSTs across S5.

Experiment SST_B is forced by the Δ_{47}-based SST record for the entire summer 6 months (Figure 7b). Overall, this represents the $\delta^{18}O$ of SML species much better than experiment SST_A. $\delta^{18}O_{universa}$ and $\delta^{18}O_{sacculifer}$ fall largely within the 95% probability envelope throughout, except at the start of S5, from 130.5 to 128.3 ka, where $\delta^{18}O_{sacculifer}$ is heavier than the model. $\delta^{18}O_{ruber}$ is mostly captured except for its most negative values ~127.3 ka in the lower lobe and at ~124 and 123 ka in the upper lobe of S5. However, as for experiment SST_A, the large amplitude change in $\delta^{18}O_{ruber}$ at the start of S5 is still not reflected in the model output. Also, in common with experiment SST_A, estimates of SML species $\delta^{18}O$ from experiment SST_B fail to capture the difference in amplitude change between $\delta^{18}O_{universa}$ and $\delta^{18}O_{ruber}$ within S5. Moreover, no distinction is found in the model output between the USML and the main body of the SML in the upper lobe. Neither SST_A nor SST_B exhibits a defined $\delta^{18}O$ signal interruption, despite monsoon freshwater runoff being switched off entirely in the model between 126.9 and 125.8 ka.

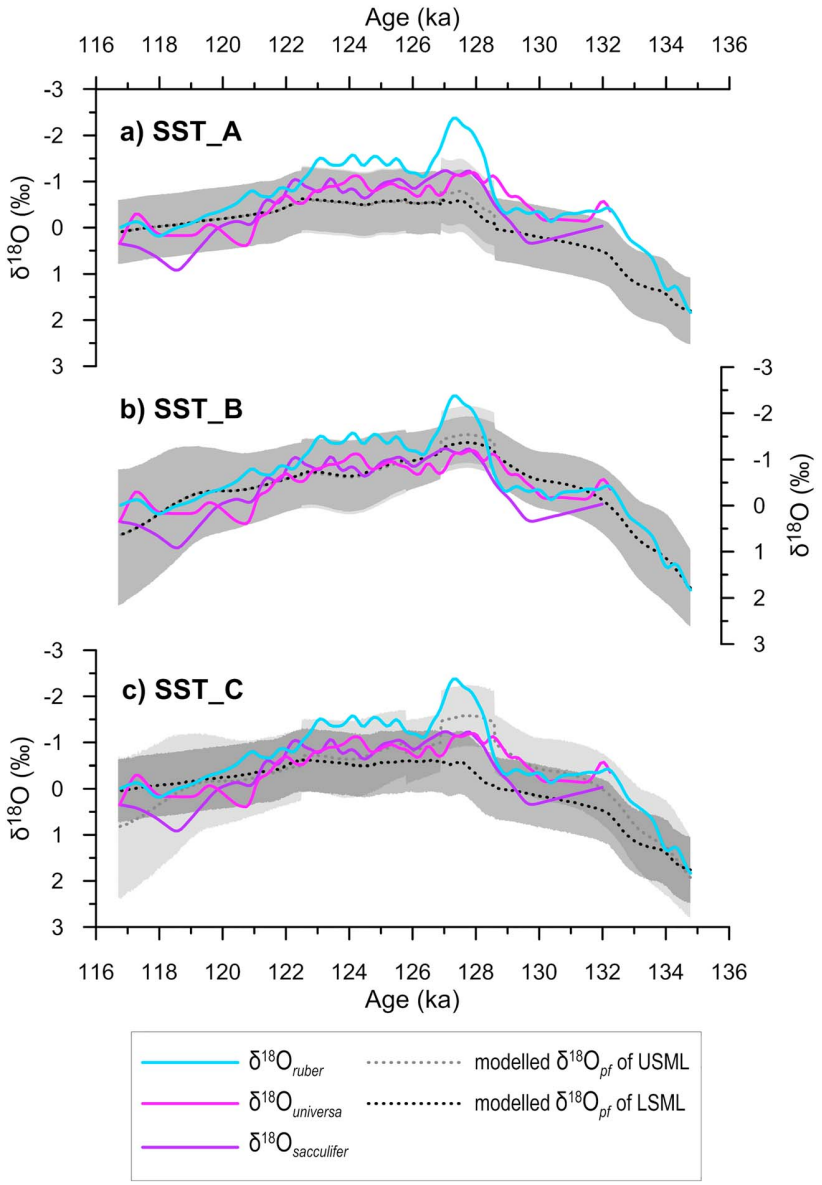

Figure 7. Results of SST diagnostic experiments (a) SST_A, (b) SST_B, and (c) SST_C. Model-predicted $\delta^{18}O$ of calcifiers for the USML (light gray) and the entire depth of the SML (dark gray). The dashed lines represent probability maxima and the shaded envelopes display the 95% probability envelopes. Model results are compared with medians of eastern Mediterranean $\delta^{18}O$ stacks for *G. ruber* (w) (blue), *O. universa* (magenta), and *G. sacculifer* (purple), as calculated from our compiled dataset and normalized to the last 3 kyr. (Note that *G. sacculifer* $\delta^{18}O$ was calculated from records for ODP 967 and LC21 only because KS205 results were anomalous for this species; see Figure 3c.)

The Δ_{47}-forced model of experiment SST_B clearly yields an improved model-data fit relative to $U^{K'}_{37}$-based SST forced experiment SST_A, but there remain some principal features observed in the $\delta^{18}O$ records that are not captured by the model. Critically, the model outputs for the freshwater-diluted USML and the main body of the SML in both experiments SST_A and SST_B fail to capture the differences observed between *G. ruber* (w) and other SML species. This suggests that the monsoon freshwater contribution alone is not enough to cause the observed differences between species residing throughout the full depth of the SML (*O. universa* and *G. sacculifer*) and *G. ruber* (w), which preferentially inhabits fresher surface waters (Rohling et al., 2004). We therefore consider that using a single SST record for the entire summer 6

months in the model does not adequately represent summer SST behavior in the eastern Mediterranean. Considering that the shallower depth habitat of *G. ruber* (w) during sapropel events is characterized by an increased freshwater contribution, which increases stratification of the SML, it would follow that the heat gained in surface waters at this time may not be mixed down through the water column to the same extent as under normal (nonmonsoon) summer conditions. Instead, concentrated warming of the freshwater-stratified USML may have caused amplification of the $\delta^{18}O_{ruber}$ signal (Emeis et al., 2003).

To account for this hypothesis about summer SST differentiation, experiment SST_C uses the $U^{K'}_{37}$-based SST record (+4 °C) to set SST of the SML over the normal 4 months of summer, and the Δ_{47}-based SST record to control the temperature of the USML during the 2 months representing the monsoon season (i.e., in the monsoon box; Figure 7c). This means that *G. ruber* (w)'s habitat is represented by the Δ_{47} measured directly on the species itself, while the remainder of the SML species are controlled by the $U^{K'}_{37}$-based SST record (+4 °C). As explained in the experimental setup, this SST forcing requires *G. ruber* (w) to be forced by a different SST to other species even when there are no enhanced African monsoon/sapropel conditions. Experiment SST_B shows that the Δ_{47}-based SST better explains presapropel and postsapropel $\delta^{18}O_{ruber}$, which suggests that *G. ruber* (w) may indeed always reside at shallower depths in the water column than other SML species and hence be more susceptible to warming.

Experiment SST_C strongly improves the model's representation of the difference between *G. ruber* (w) and *O. universa* in the model outputs for the freshwater-diluted USML and the main body of the SML (Figure 7). Studied individually, experiment SST_B agrees better with the $\delta^{18}O_{universa}$ than experiment SST_C in terms of absolute values. However, amplitude changes between species are more reliable to examine in this study than absolute $\delta^{18}O$ values, and relative amplitude variations are better represented by experiment SST_C. Experiment SST_C better captures the sudden $\delta^{18}O_{ruber}$ shift to low values at the start of S5, although modeled $\delta^{18}O$ still does not reach the full extent of $\delta^{18}O$ depletion exhibited by *G. ruber* (w). In fact, all of the model runs presented so far fail to capture the full amplitude change observed in $\delta^{18}O_{ruber}$ over S5, which suggests that monsoon freshwater inputs during S5 may have been underestimated in the model. Still, these experiments were about diagnosing which SST approach to take, not about quantifying monsoon intensification (that will be done in section 6).

5.2. USML Depth Diagnostics

In the box model, the impact of excess freshwater runoff input during S5 relates to both the volume and $\delta^{18}O$ of monsoon runoff. Moreover, the influence on the $\delta^{18}O$ of the surface layer depends on the set depth of the USML (i.e., the volume into which freshwater input is initially mixed). The resultant seawater $\delta^{18}O$ and SST during the monsoon season (i.e., the temperature of the USML) are then used to calculate the expected $\delta^{18}O$ for calcifiers in the USML (i.e., *G. ruber* (w)). In the model, the excess freshwater runoff, SST, and depth of the USML during the monsoon season are distinct, separately defined parameters. However, in the real world, these parameters would be considerably interrelated. Of these, SST is the only parameter independently measured for S5, while monsoon runoff volume and depth of the USML have only been roughly approximated using a simpler, earlier version of the model applied here (Rohling et al., 2004). Using observations made during our SST diagnostics, we can now refine some of the relationships between these parameters.

The SST diagnostics suggest that the Δ_{47}-*G. ruber* (w) SST record reflects the SST of the USML, while the $U^{K'}_{37}$-based SST with a superimposed seasonal deviation (+4 °C) reasonably reflects the temperature of the main body of the SML. Building on this concept of surface water stratification during S5, we calculate the difference between the Δ_{47}-based and $U^{K'}_{37}$-based (+4 °C) SST records over the study interval (ΔT; Figure 5), to approximate the temperature difference between the USML and LSML.

We then set up a correlation between ΔT and the depth of the USML to estimate the USML depth throughout S5 from the SST data. This relationship assumes that if $\Delta T = 0$, when both the Δ_{47} and $U^{K'}_{37}$ records show the same SST, there is no separation of the SML into an USML and LSML. In that case, the assumption is that *G. ruber* (w) no longer has the fresher surface water niche to exploit and is residing in the main body of the SML. Hence, when $\Delta T = 0$, the depth of the USML is set to 30 m (the full SML depth; D'Ortenzio et al., 2005). On the other hand, as ΔT increases, we interpret this as a greater temperature concentration effect in the USML; that is, there is a thinner, fresher, more stratified layer over which insolation warming is

concentrated. To represent this increase in stratification, we decrease the depth of the USML with increasing ΔT, which concentrates the freshwater influences. The minimum stratification depth for the USML is unknown, and different scenarios are explored in the following set of experiments. A linear relationship is then assumed between the two end-members.

5.2.1. Experimental Setup

We set up three experiments to test the validity of the above concept that the depth of the USML may be approximated from ΔT in the Mediterranean box model (experiments zUSML_A, zUSML_B, and zUSML_C; Table 3). Each experiment is set up with a different minimum USML stratification depth when ΔT is at the maximum observed during the S5 interval (5.7 °C; Figure 5). We then establish equations for each experiment, which define the linear increase in USML depth from the prescribed minimum to a maximum of 30 m, as ΔT decreases from 5.7 to 0 °C (Table 3). All other parameters in these experiments were kept constant, as defined in experiment SST_C. This isolates the impacts of changing the USML depth with ΔT on the simulated $\delta^{18}O$ profiles.

Experiment zUSML_A uses a minimum USML depth of 1.5 m. This draws on calculations by Rohling et al. (2004) that 1.5 m is the shallowest USML depth before salinity becomes too low to be able to sustain foraminiferal life (~22 p.s.u). In the present model, salinities do not fall this low for an USML depth of 1.5 m because evaporation over a thin, very warm surface layer removes much of the freshwater. However, reducing USML depths to less than 1.5 m causes the model's evaporation-precipitation-runoff balance to become unstable and produce singularities in the $\delta^{18}O$ estimates. Therefore, 1.5 m is still used as the shallowest minimum USML depth. Experiment zUSML_B has a minimum USML depth of 5 m, which corresponds to the initial depth suggested by Rohling et al. (2004) and which was used throughout the entire sapropel interval in our SST diagnostic experiments. Lastly, experiment zUSML_C uses a deeper minimum USML depth of 10 m.

The results of these experiments are compared with the S5 $\delta^{18}O_{ruber}$ data alongside the results of SST diagnostics experiment SST_C, which is identically constrained except that the depth of the USML is set at a constant 5 m throughout (Table 3). This will determine if varying the depth of the USML with ΔT offers an improvement to the simulated $\delta^{18}O_{ruber}$.

5.2.2. Results

The expected $\delta^{18}O$ for calcifiers in the USML in experiments zUSML_A, zUSML_B, and zUSML_C are virtually identical throughout the study interval, with differences only discernible in the lower lobe of S5 from 129 to 127.5 ka (Figure 8). In the lower lobe, zUSML_A simulates the most negative $\delta^{18}O$ anomaly, reaching −1.7‰ at the onset of S5 at 128.3 ka, which corresponds to the time of greatest ΔT. The simulated $\delta^{18}O$ of the lower lobe is more positive in zUSML_B, and even more so in zUSML_C. However, overall, the three experiments vary by less than 0.3‰ at their maximum, well within uncertainties, indicating a stability of the system with regard to changes in depth of the USML. The greatest differences are seen over the lower lobe of S5 because ΔT is greatest over this interval, and USML depth in each experiment approaches its respective minimum value (Figure 8a). As ΔT decreases toward 0, the estimated USML depths for all experiments attenuate to 30 m. Furthermore, as the depth of the USML increases, the effect of surface hydrological processes is increasingly diluted (e.g., a difference between 1.5 and 5 m in USML depth more than triples the volume into which freshwater is added, whereas a difference of 3.5 m at greater depths makes a proportionally smaller difference).

Overall, the calculated $\delta^{18}O$ changes for *G. ruber* (w) in experiments zUSML_A, zUSML_B, and zUSML_C are very similar to those of SST_C (Figure 8b). The greatest difference is observed over nonsapropel intervals (i.e., pre-S5, the freshwater runoff interruption, and post-S5). In SST_C, the depth of the USML remains at 5 m throughout the study interval. As the Mediterranean is an evaporative basin, under normal conditions there is an excess of evaporation over precipitation runoff. Therefore, in SST_C when the enhanced monsoon runoff is switched off during nonsapropel intervals, the net evaporative loss is still concentrated over a thin surface layer, without any offset from increased freshwater input. This excess evaporation preferentially removes light ^{16}O, increasing the $\delta^{18}O$ of the USML. The calculated $\delta^{18}O$ from experiments zUSML_A, zUSML_B, and zUSML_C generally shows better visual agreement than SST_C with the $\delta^{18}O_{ruber}$ data, implying that an USML depth that is set to vary with ΔT somewhat better captures the conditions in the eastern Mediterranean basin during S5.

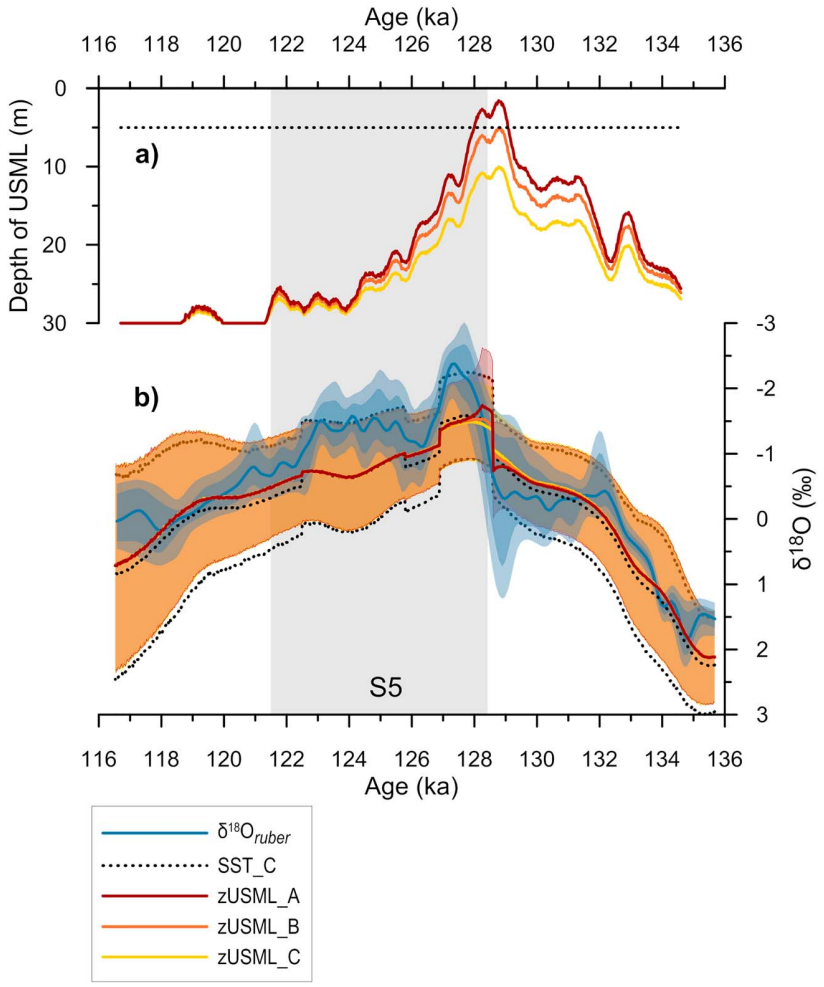

Figure 8. Results of depth of USML diagnostic experiments. Depth constraints of USML and model-predicted $\delta^{18}O$ of calcifiers for the USML for diagnostic experiments zUSML_A (red), zUSML_B (orange), zUSML_C (yellow), and SST_C (dashed black). Medians (solid lines/heavy dashed), 95% confidence limits (shaded envelopes/light dashed). Model results are compared with eastern Mediterranean $\delta^{18}O$ stack for *G. ruber* (w) (blue), median (solid line), and 68% and 95% confidence limits (shaded envelopes). S5 interval (gray shaded band).

6. Calculation of African Monsoon Runoff

6.1. Box Model Inversion

Our modeling of the Mediterranean system in the diagnostic experiments (section 5) was restricted over sapropel intervals by the limited resolution of monsoon runoff, which was simplified to an on/off switch from a normal state to an intensified African monsoon state. In reality, the volume of monsoon runoff is likely variable and transitions more gradual than the on/off switch. However, by using ΔT to define the USML depth in the model (section 5.2), the only remaining major unquantified parameter that exerts a control over the expected $\delta^{18}O$ of calcifiers in the USML is the actual volume of monsoon freshwater runoff. Therefore, it becomes possible to invert the box model and for the volume of monsoon freshwater runoff into the Mediterranean to become the calculated output.

The inverted model uses the eastern Mediterranean $\delta^{18}O_{ruber}$ stack with its full probability distribution as an input to constrain the $\delta^{18}O$ of USML calcifiers. Other paleoproxy records used as model inputs (i.e., sea level and SST records) were kept the same as for experiment SST_C and the zUSML experiments (Table 3). The $\delta^{18}O$ of excess monsoon freshwater runoff during S5 is again varied randomly within its range of possible values (−8% to −12‰), as before (section 5). The relationship between ΔT and the depth of the USML

could not be definitively defined through diagnostic experiments (section 5.2), so a randomizer is used to allow for a range of possible relationships to be considered in the model, (i.e., at maximum ΔT, minimum depth of the USML varies between 1.5 and 10 m).

While the structure of the box model remains very similar, some equations within the inverted model have been rearranged to correspond to the new inputs and outputs of the model. To enable this, two parameters previously calculated by the model needed to be simplified. First, the residence time of the LSML is taken to be the same as calculated by the original box model (set up as for experiment SST_C; section 5.1). The residence time of the LSML varies predominantly with sea level, which does not change between different model runs; hence, this is a valid approximation. Second, shoaling of the pycnocline (which separates the surface and intermediate waters) during sapropel deposition (Rohling, 1991; Rohling & Gieskes, 1989) is simplified according to ΔT. When $\Delta T > 0$ (based on our working hypothesis that this marks freshwater-induced stratification), the depth of the winter mixed layer is set to ~100 m (after Rohling, 1991; Rohling et al., 2004). When $\Delta T \leq 0$ (SML is not split into USML and LSML, and basin conditions are normal), the depth of these layers is set to ~150 m, which is the normal depth of the winter mixed layer during the present day (Nykjaer, 2009; Rohling, 1991). The depth of the summer subthermocline and winter mixed layers does not affect calculations of the monsoon freshwater runoff volume, so this approximation is acceptable for the purpose of quantifying African monsoon runoff in this study.

6.2. Atlantic Freshwater Influence During Heinrich Stadial 11

In the Mediterranean box model, the seawater $\delta^{18}O$ of Atlantic inflow to the Mediterranean is calculated according to sea level using a function of the present inflow value to account for glacial enrichment of ocean $\delta^{18}O$ (Figure 9b). However, prior to sapropel event S5, flow of Atlantic water into the Mediterranean is thought to have been significantly increased in association with North Atlantic cold event Heinrich Stadial 11 (HS11, ~135–130 ka; Sierro et al., 2005; Jiménez-Amat & Zahn, 2015; Marino et al., 2015; Grant et al., 2016; Rodríguez-Sanz et al., 2017). HS11 coincided with a deglacial meltwater pulse, adding isotopically light freshwater into the subpolar North Atlantic, which was likely circulated toward the Gulf of Cadiz by the Canary Current (Swingedouw et al., 2013). Isotopic depletions have been detected in the $\delta^{18}O$ of western Mediterranean surface waters for the HS11 interval, indicating the influence of fresher Atlantic waters at this time (Jiménez-Amat & Zahn, 2015; Marino et al., 2015; Rodríguez-Sanz et al., 2017; Sierro et al., 2005). If the isotopically light surface waters reached the eastern Mediterranean, this may influence the $\delta^{18}O_{ruber}$ signals in the basin and would need to be accounted for in order to avoid biasing the African monsoon runoff calculation.

In the first model run, African monsoon runoff is calculated without consideration of an Atlantic freshwater influence during HS11. In the second model run, we constrained the seawater $\delta^{18}O$ of Atlantic inflow in the Mediterranean box model over the HS11 interval (Figure 9b). We restricted the prescribed HS11 Atlantic inflow to the Mediterranean to 135 (±1) to 130 (±2) ka, as negative seawater $\delta^{18}O$ and SST cooling anomalies have been observed during this interval in western Mediterranean sites, which have been tuned to the same age model as used here (Marino et al., 2015; Martrat et al., 2014; Rodríguez-Sanz et al., 2017). To constrain the Atlantic $\delta^{18}O$ during this interval, we used a seawater $\delta^{18}O$ record from site MD01-2444 on the Iberian margin, which is located on the path of the Canary current (Figure 9b, Skinner & Shackleton, 2006). Due to mixing of surface waters, straight use of an isotopic depletion from the Iberian Margin most likely overestimates the isotopic influence of Atlantic freshwater on the Mediterranean during HS11. However, this provides an extreme case of HS11 influence to compare with the original model run, which has no imposed isotopic anomaly in Atlantic inflow. Uncertainties in both seawater $\delta^{18}O$ of Atlantic inflow and age constraints are included and propagated through the model (see section 3.6).

6.3. Results

Our calculated African monsoon runoff is presented both in terms of total monsoon runoff volume and of a monsoon intensification factor relative to *present-day* African runoff (Figure 9c). Present-day African runoff is almost entirely derived from the Nile (Struglia et al., 2004), which here is taken to be 1.5×10^{11} m^3/year, based on modern Nile River discharge in a high-flood year, prior to Aswan damming (Rohling et al., 2015).

Prior to S5, the calculated monsoon runoff median is low, generally at or below the volume of present-day runoff. At ~134 ka, the calculated monsoon runoff median is less than 0 m^3, reaching a minimum of ~

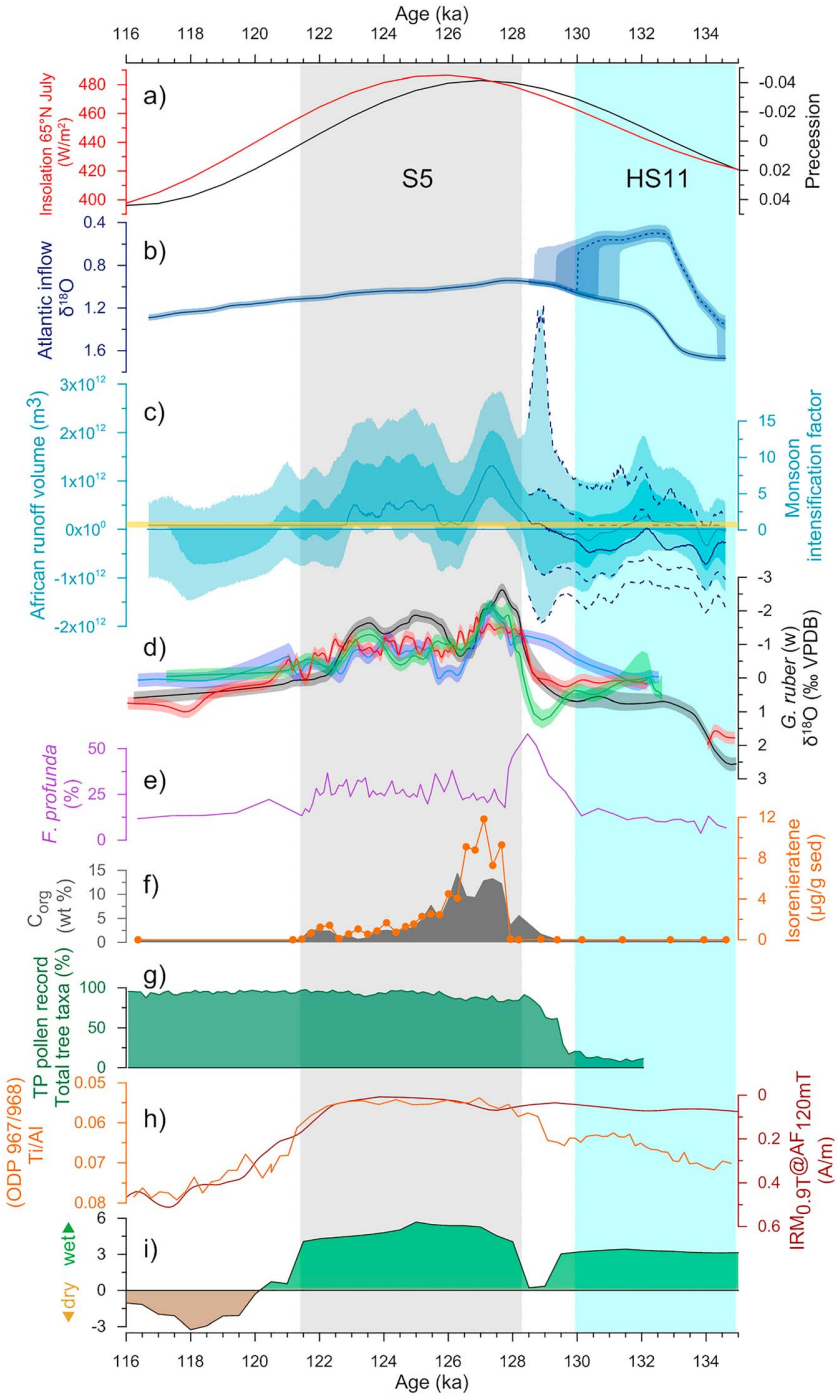

Figure 9. African monsoonal runoff and other regional proxy records. (a) Insolation in mid-July at 65°N and precession index (Berger & Loutre, 1991), (b) Atlantic inflow $\delta^{18}O$ used in inverted model as calculated according to sea level (solid), and with HS11-associated negative $\delta^{18}O$ anomaly (dashed; Skinner & Shackleton, 2006; age constraints: Jiménez-Amat & Zahn, 2015; Marino et al., 2015), 68% and 95% confidence intervals (shaded envelopes), (c) African monsoonal runoff estimate (blue), median (solid line), 68% and 95% confidence intervals (shaded envelopes). African monsoonal runoff estimate when accounting for HS11 with Atlantic freshwater addition (dark blue), median (solid line), 68% and 95% confidence intervals (dotted lines), yellow band indicates modern range of pre-Awan Nile runoff volume (based on Rohling et al., 2015), (d) $\delta^{18}O_{ruber}$ for ODP 967 (green), LC21 (red), KS205 (blue) and ODP 971 (black), median (solid line), 95% confidence intervals (shaded envelopes), (e) percent *F. profunda* in LC21 (purple; Grelaud et al., 2012), (f) weight percent organic carbon in LC21 (C_{org}; gray; Marino et al., 2007), Isorenieratene concentration in LC21 (orange; Marino et al., 2007), (g) total tree-pollen taxa record from Tenaghi Philippon in Greece (dark green; Milner et al., 2012, 2016; Wulf et al., 2018), (h) Ti/Al record from ODP967/968 (orange; Konijnendijk et al., 2014), $IRM_{0.9T}@AF_{120mT}$ record from ODP 967 (dark red; Larrasoaña, Roberts, Rohling et al., 2003), (i) wet-dry index from ODP 967 (Grant et al., 2017). S5 interval (gray-shaded band), timing of HS11 (blue shaded band; Marino et al., 2015).

-3.3×10^{11} m^3 (Figure 9c). Thereafter, from ~131.3 to 129 ka, there is a distinct interval of reduced monsoon runoff to less than the present day, reaching a minimum at ~130.4 ka. In the additional model run, which switches on an isotopically light Atlantic freshwater inflow associated with HS11 (from 135 ± 1 to 130 ± 2 ka), the monsoon runoff estimate over this interval is even further decreased, with negative median monsoon runoff volumes throughout almost all the HS11 interval (Figure 9c). Potential explanations for these negative monsoon runoff estimates are discussed in section 7.3.

Estimated African monsoon runoff during S5 indicates two main intervals of elevated freshwater runoff into the Mediterranean at 128.5–126.5 ka and 125.7–122.8 ka, which correspond to the lower and upper lobes in the S5 $\delta^{18}O_{ruber}$ records, respectively (Figures 9c and 9d). The onset of S5 at 128.3 ka (as defined by Grant et al., 2016) immediately follows a sharp increase in monsoon runoff volume, which reaches a peak at ~8.8 times the total present-day runoff (~1.3×10^{12} m^3) at 127.4 ka. Following this peak, monsoon runoff decreases to a temporary minimum at 126.5–125.7 ka, when median runoff volume approximates the present-day value. This interval corresponds to the *interruption* observed in $\delta^{18}O_{ruber}$ records for ODP 971 and KS205 (Figure 9d) and noted by previous studies (e.g., Rohling et al., 2002, 2004; Scrivner et al., 2004). Monsoon runoff then increases into the upper lobe, where median values fluctuate between ~1.6 and 4 times monsoon intensification (2.4–6.1 $\times 10^{11}$ m^3) relative to the present day. At 122.8 ka, the median monsoon runoff decreases to present-day equivalent values, approximately 1.2 kyr before the end of S5 deposition at 121.5 ka.

7. Discussion

7.1. $\delta^{18}O$ Sapropel Imprint

7.1.1. Freshwater Source

African monsoonal runoff is widely acknowledged as a source of isotopically light freshwater to the eastern Mediterranean during sapropel events (e.g., Hennekam et al., 2014; Larrasoaña, Roberts, Stoner, et al., 2003; Lourens et al., 2001; Osborne et al., 2008, 2010; Rohling et al., 2004, 2015; Rossignol-Strick, 1985). However, increased outflow of fresher waters from the Black Sea (Lane-Serff et al., 1997; Olausson, 1991) and increased winter precipitation along the northern borderlands of the eastern Mediterranean (e.g., Kotthoff et al., 2008; Kutzbach et al., 2014; Milner et al., 2012) have been proposed as potential additional freshwater sources.

Our $\delta^{18}O_{pf}$ data sets compiled from four eastern Mediterranean core sites (Figures 1 and 3) are well located to monitor the source location, and subsequent circulation, of freshwater inputs to the basin during the S5 interval. Of the four cores included in this study, the most negative $\delta^{18}O_{ruber}$ signal for S5 is in ODP Site 971 (Figure 9d), which is the closest site to the African margin. The present-day antiestuarine circulation of the Mediterranean is thought to have been maintained during sapropel events, including S5 (Incarbona et al., 2011; Myers et al., 1998; Rohling, 1994). Consequently, anticlockwise surface circulation in the eastern Mediterranean would have been similar to the present (Figure 1b). Therefore, assuming that there were no major freshwater sources in the western Mediterranean, a freshwater signal at ODP 971 would have to originate from the African margin. This suggests that the greatest freshwater input to the eastern basin during S5 entered the basin via paleoriver systems along the North African margin, rather than from the Nile. ODP 967 is located close to Nile outflow (Figure 1b) and shows the second greatest depletion in $\delta^{18}O_{ruber}$ (Figure 9d). While a large part of the freshwater signal in ODP 967 may be sourced from the Nile, as this site lies in the path of surface water circulation traveling eastward, it would also receive some isotopically light freshwater originating from drainage along the wider African margin.

Currently, the Po has the greatest river discharge from Europe into the eastern Mediterranean (Ludwig et al., 2009). Increased winter precipitation over the northern borderlands would be expected to have increased the runoff from the Po into the Adriatic. Core site KS205 is located just south of the Adriatic, so it would potentially record freshwater influences as surface circulation transports the fresher, more buoyant water into the main basin (Figure 1). However, there is no evidence of a greater freshwater influence in the winter mixed layer at KS205, with $\delta^{18}O_{siphonifera}$ virtually the same for all core sites included in the study (Figure 3d). $\delta^{18}O_{sacculifer}$ is more negative in KS205 than any other core, but this is not the case in $\delta^{18}O_{ruber}$ and $\delta^{18}O_{universa}$, so there is also no evidence of greater freshwater influence in the SML (Figures 3a–3c). Likewise, we would expect an increased outflow of fresher waters from the Black Sea to be evidenced by low anomalies in $\delta^{18}O_{pf}$ in LC21, which is located in the southern Aegean (Figure (1). However, LC21

does not exhibit more negative $\delta^{18}O$ in any surface mixed layer species compared to the other eastern Mediterranean cores (Figures 3a–3d). Therefore, while we cannot exclude freshwater contributions from the Black Sea or European borderlands, our multisite comparison shows no evidence of major contributions from these sources and instead supports previous observations (Osborne et al., 2010) that these were negligible in comparison to the African-sourced freshwater during the development of S5.

7.1.2. Temperature Versus Freshwater Influence on $\delta^{18}O_{ruber}$

The eastern Mediterranean Δ_{47}-*G. ruber* (w) SST stack indicates SSTs higher by up to 5.7 °C than summer temperatures inferred from the $U^{K'}_{37}$-based SST stack during the study interval (Figure 5). The model can only reproduce the observed $\delta^{18}O$ difference between *G. ruber* (w), which opportunistically shifts into lower salinity surface waters during periods of monsoon flooding, and other SML species that remain in the main body of the SML, when accounting for a higher SST for *G. ruber* (w; i.e., the Δ_{47}-based SST record). This indicates that both stratification of the SML and a temperature concentration effect within the surface layer (cf. Emeis et al., 2003 ; Rodríguez-Sanz et al., 2017) are necessary to describe the amplified depletion of $\delta^{18}O_{ruber}$ relative to other planktic species during S5.

Besides this temperature concentration effect, the freshwater influence on planktic $\delta^{18}O$ during sapropels is also clearly important. Simulated $\delta^{18}O$ in the SST diagnostics were not low enough to replicate the $\delta^{18}O_{ruber}$ observations (Figure 7), which indicates that previous estimates of freshwater runoff volumes during S5 (Rohling et al., 2004) were too low. Rohling et al. (2004) suggested a monsoon intensification equivalent to 160–300% of the total present-day runoff into the Mediterranean for the lower lobe and 120–200% the present-day runoff for the upper lobe. In this study we report monsoon intensification as a factor of the present-day Nile discharge (see section 6.3), rather than total runoff, which would bring the Rohling et al. (2004) estimates to 2.4–6.6 and 1.2–3.6 African monsoon intensification for the lower and upper lobes, respectively. Our calculated African monsoon runoff from the inverted model approach is considerably higher (Figure 9c), with our most probable monsoon intensification estimates reaching 8.8 times the present day in the lower lobe and 1.6–4 times the present day in the upper lobe. Rohling et al.'s (2004) estimates were likely lower than ours because they were based on the $\delta^{18}O_{ruber}$ record from KS205, while this study accounts for KS205 together with three additional eastern Mediterranean cores. The multisite $\delta^{18}O_{ruber}$ comparison (Figure 9d) shows that KS205 $\delta^{18}O_{ruber}$ anomaly is smaller than those in cores ODP 967 and ODP 971. This highlights the advantage of using multiple sites to provide a more comprehensive insight to the eastern Mediterranean. The eastward circulation of surface waters along the African coast gives us assurance that any freshwater entering the eastern Mediterranean from Africa will be recorded to some extent in the $\delta^{18}O_{ruber}$ signals of ODP 971, ODP 967, and even the cores further along the circulation pathway. With our core sites located at key points for surface circulation around the eastern Mediterranean (Figure 1b), we are confident in a good overall representation of the basin.

Our stacked eastern Mediterranean $\delta^{18}O_{ruber}$ and SST records from spatially distributed sites are taken to represent basin averages. Likewise, our box model differentiates Mediterranean water masses by depth and season, but they remain horizontally homogeneous. However, $\delta^{18}O_{ruber}$ can differ quite substantially through S5 at the four sites considered here (Figure 9d). These differences reflect both differences in freshwater influence and SST at the individual sites. If SST could be accounted for separately for each eastern Mediterranean site, then the freshwater influence on $\delta^{18}O_{ruber}$ could be isolated for each. This would provide further information on the circulation and attenuation of freshwater within the eastern basin. $U^{K'}_{37}$-based SST reconstructions are available for all the sites included in this study and show little spatial variation (Marino et al., 2007; Rohling et al., 2002, 2004). However, the Δ_{47}-*G. ruber* (w) SST reconstructions are only available for ODP 967 and LC21 and show larger differences (Rodríguez-Sanz et al., 2017). ODP 967 and LC21 are the two easternmost sites in the study (Figure 1), so we may expect the other two sites (ODP 971 and KS205) to show even greater Δ_{47}-*G. ruber* (w) SST differences, given the present-day Mediterranean SST gradient (Locarnini et al., 2010). Greater spatial coverage with Δ_{47}-*G. ruber* (w) records will help with better quantification of mixing and freshwater circulation and of monsoon freshwater input locations and volumes.

7.2. African Monsoon Runoff

The calculated African monsoon runoff presented here (Figure 9c) represents the first continuous record of quantified excess freshwater influx into the eastern Mediterranean during S5 deposition. All features of the

African monsoon runoff reconstruction over the S5 interval are responses solely to the input records. We compared these results with an additional model run in which an isotopically depleted Atlantic inflow was imposed in the model from 135 (±1) to 130 (±2) ka to account for Atlantic freshwater entering the Mediterranean during HS11 (section 6.2). We discuss the various results in the following sections. The generously calculated monsoon runoff uncertainty accounts for full propagation of errors from the multiple inputs and parameters in the model, and the signal determined in the monsoon runoff reconstruction is robust relative to these uncertainties. There is a large *spike* increase in the 95% confidence envelope of the calculated African monsoon runoff at ~129 ka (Figure 9c), which corresponds to two features in the input records, which increase uncertainty: (a) the interval of largest uncertainty in the $\delta^{18}O_{ruber}$ stack (Figure 6a) and (b) the greatest ΔT (Figure 5c), which is associated with the thinnest USML through the defined relationship in the model (where small differences in USML thickness arising from Monte Carlo sampling would make the greatest difference proportionally; section 5.2).

7.2.1. Sapropel Onset

The clearly defined increase in monsoon intensity from ~128.5 ka (Figure 9c), corroborated by rapid increases in terrigenous supply in the Nile outflow region (Dirksen et al., 2019), is some 200 years before the start of S5 deposition at ~128.3 ka (Grant et al., 2016). This indicates a very rapid development of basin conditions to enable sapropel preservation following increased freshwater influx to Mediterranean surface waters. However, the median ΔT is greater than 0 °C from the start of the study interval at ~135 ka (Figure 5c), which, according to our working hypothesis, indicates SML stratification and formation of the USML. This suggests that eastern Mediterranean surface water stratification increased from ~6.7 kyr before the increase in monsoon freshwater influx into the basin. Prior to Holocene sapropel S1, stratification was likely encouraged by Mediterranean surface water freshening due to both rapid sea level rise and freshening of Atlantic inflow and concomitant glacial to interglacial SST increases (Grant et al., 2016; Grimm et al., 2015; Matthiesen & Haines, 2003). Similarly, before S5, an increase in stratification may have been driven by Atlantic freshening associated with HS11, as well as rapid sea level rise and increasing SSTs associated with Termination II, which accelerated ~133 ka (Figure 5; Grant et al., 2012), following an onset as early as 135 ka (Marino et al., 2015). Cold, salty glacial waters would have filled the Mediterranean basin prior to the start of the glacial termination, enhancing the potential for stratification during these events due to the density contrast with fresher incoming surface waters (Emeis et al., 2003). Increased stratification before the onset of S5 is also supported by an increasing abundance of the lower photic zone coccolithophore *Florisphaera profunda* in LC21 from ~130 ka until the start of the S5 interval (Figure 9e; Grelaud et al., 2012, using Grant et al., 2012, LC21 age model). *F. profunda* indicates the development of a deep chlorophyll maximum (DCM), which is associated with pycnocline shoaling and increasing stratification. Total organic carbon (C_{org}) preserved in LC21 increases from ~129.5 ka (Figure 9f; Marino et al., 2007, using Grant et al., 2012, LC21 age model), which may evidence an increase in export production fuelled by a DCM before the onset of S5. Together, this evidence for an increase in stratification and productivity prior to the start of the calculated African monsoon runoff suggests a considerable sequence of preconditioning of the eastern Mediterranean for the development of anoxic conditions.

During S5, euxinic conditions extended up to the base of the photic zone, reaching an estimated ~200 m in the Aegean Sea at ~127.9 ka (Marino et al., 2007, using Grant et al., 2012, LC21 age model). This is evidenced by high concentrations of isorenieratene (Figure 9f), which indicates the presence of anaerobic, phototrophic green sulphur bacteria (Chlorobiaceae), which require both sulphide and light (Koopmans et al., 1996; Passier et al., 1999; Repeta et al., 1989; Rohling et al., 2006). Based on modern oxygen utilization rates, consumption of all oxygen below 500-m depth is estimated to take 640 years following a collapse of deep water formation (Rohling, 1994). However, during S5, oxygen below ~200 m is consumed just 600 years after the calculated African monsoon runoff starts to increase, and exceeds present-day volumes. With the same oxygen utilization as the present day, these timings require an abrupt cessation of deep water formation immediately following the increase in monsoon freshwater influx to the basin. Higher levels of productivity would have aided a rapid oxygen utilization and extension of euxinic conditions in the eastern Mediterranean following a collapse of deep water formation, which may explain the rapid onset of sapropel deposition observed. However, modeling studies for S1 indicate that even with enhanced production (3x increase in nutrient influx) and strong density stratification, deep water anoxia takes at least 3.4 kyr to develop in the eastern Mediterranean (Grimm et al., 2015). This suggests the above estimates of complete

oxygen consumption below the photic zone in <1,000 years may be greatly underestimated and supports a preconditioning of the eastern Mediterranean as a requirement for the observed onset of S5 deposition.

7.2.2. African Monsoon Runoff Interruption

During the $\delta^{18}O_{ruber}$ signal interruption (126.5–125.7 ka), the median calculated African monsoon runoff is the same as the present-day (pre-Aswan) Nile runoff into the Mediterranean (Figure 9c). This reduction in runoff volume during the interruption could be explained by a southward shift in the summer Intertropical Convergence Zone (ITCZ) midway through S5, to a position south of the Saharan watershed. A prominent North Atlantic cooling event associated with a meltwater event off of Greenland has been identified ~126.5–125 ka and may be responsible (Irvalı et al., 2012; Salonen et al., 2018; Zhuravleva et al., 2017). This ITCZ shift may have prevented the African monsoon from penetrating the Saharan watershed and caused a shutdown of the paleodrainage systems along the wider African margin, as all the runoff during this interval can be accounted for by a Nile outflow similar to the present day (pre-Aswan). When African monsoon runoff increased again, ending the interruption at ~125.7 ka, the $\delta^{18}O_{ruber}$ in ODP 971 started to decrease (Figure 9d), suggesting a reactivation of the paleodrainage systems along the North African margin. However, ODP 967 $\delta^{18}O_{ruber}$ does not decrease again until ~124 ka, which suggests that Nile discharge stayed at the same levels as during the interruption. Furthermore, eastward surface circulation would be expected to transport freshwater from the African margin to ODP 967 (Figure 1b), but there is no evidence of this in ODP 967 $\delta^{18}O_{ruber}$. However, as seen in the SST diagnostic experiments (section 5.1), temperature also has an important influence on $\delta^{18}O_{ruber}$, in particular during S5 when a temperature concentration effect is observed for the thin, freshwater-diluted USML. The Δ_{47}-based SST, which is measured directly on *G. ruber* (w), indicates a lower temperature for the latter half of S5 (Figure 5b), and in particular, SST for ODP 967 is 1–3 °C lower than for LC21 from 126 to 121.5 ka (Rodríguez-Sanz et al., 2017). This partly explains the observations of $\delta^{18}O_{ruber}$ for ODP 967. Again, this emphasizes the importance of considering temperature when studying $\delta^{18}O_{ruber}$ over sapropel events and in particular highlights the value of targeting future Δ_{47}-based SST reconstructions on sites in close proximity to ODP 971 for tracing freshwater circulation within the basin.

Interestingly, of the four cores in this study KS205 displays the most pronounced $\delta^{18}O_{ruber}$ signal interruption from 126.5 to 125.7 ka (Figure 9d), despite being the farthest site from African runoff sources. This may indicate that during this interval, when African runoff decreased to volumes similar to the present day, the freshwater influx was not enough to circulate the eastern Mediterranean and reach KS205 as a distinct surface signal but is instead attenuated into the water column before reaching the north Ionian Sea (Figure 1b). In this case, stratification of the SML in the northern Ionian may have broken down, with $\delta^{18}O_{ruber}$ reflecting the $\delta^{18}O$ of the entire SML rather than just the USML. However, KS205 $\delta^{18}O_{universa}$ over this interval also increases (Figure 3b), suggesting that the increase in $\delta^{18}O_{ruber}$ is not only due to a mixing down of the USML, but at least partly due to other influences. KS205 may have undergone a regional cooling associated with the North Atlantic cooling event; although if there was a regional SST decrease at this time, it appears to be restricted to summer, as neither the $U^{K'}_{37}$-based SST nor $\delta^{18}O_{siphonifera}$ for KS205 show any significant change during the interruption interval (Figures 3d and 4a). As discussed previously, precipitation over the northern borderlands and associated runoff cannot be excluded as an influence over this period (section 7.1.1.) but without further constraint is difficult to account for. Again, a *G. ruber*-Δ_{47} SST reconstruction would be valuable for the North Ionian region of KS205, not only to investigate a possible summer cooling over this interval but also to study the site-specific ΔT to deduce the regional state of SML stratification through S5.

7.3. Mediterranean Aridity/Humidity

Estimated African monsoon runoff for the pre-S5 interval is mostly below present-day levels (Figure 9c), suggesting more arid conditions over North Africa and a reduction in Nile outflow. A negative median monsoon runoff volume is calculated for ~134 ka and ~131–129 ka in the model run without an imposed Atlantic freshening, and throughout almost the entire HS11 interval in the additional model run with an imposed Atlantic freshening. While negative runoff is not physically possible, it does not immediately invalidate the results. The model assumes that runoff from non-African rivers (~3.7×10^{11} m^3/year) remains the same proportionally to precipitation. While a relative decrease in non-African runoff could compensate for part of the negative runoff calculated during HS11, it cannot fully account for the negative median volume in either

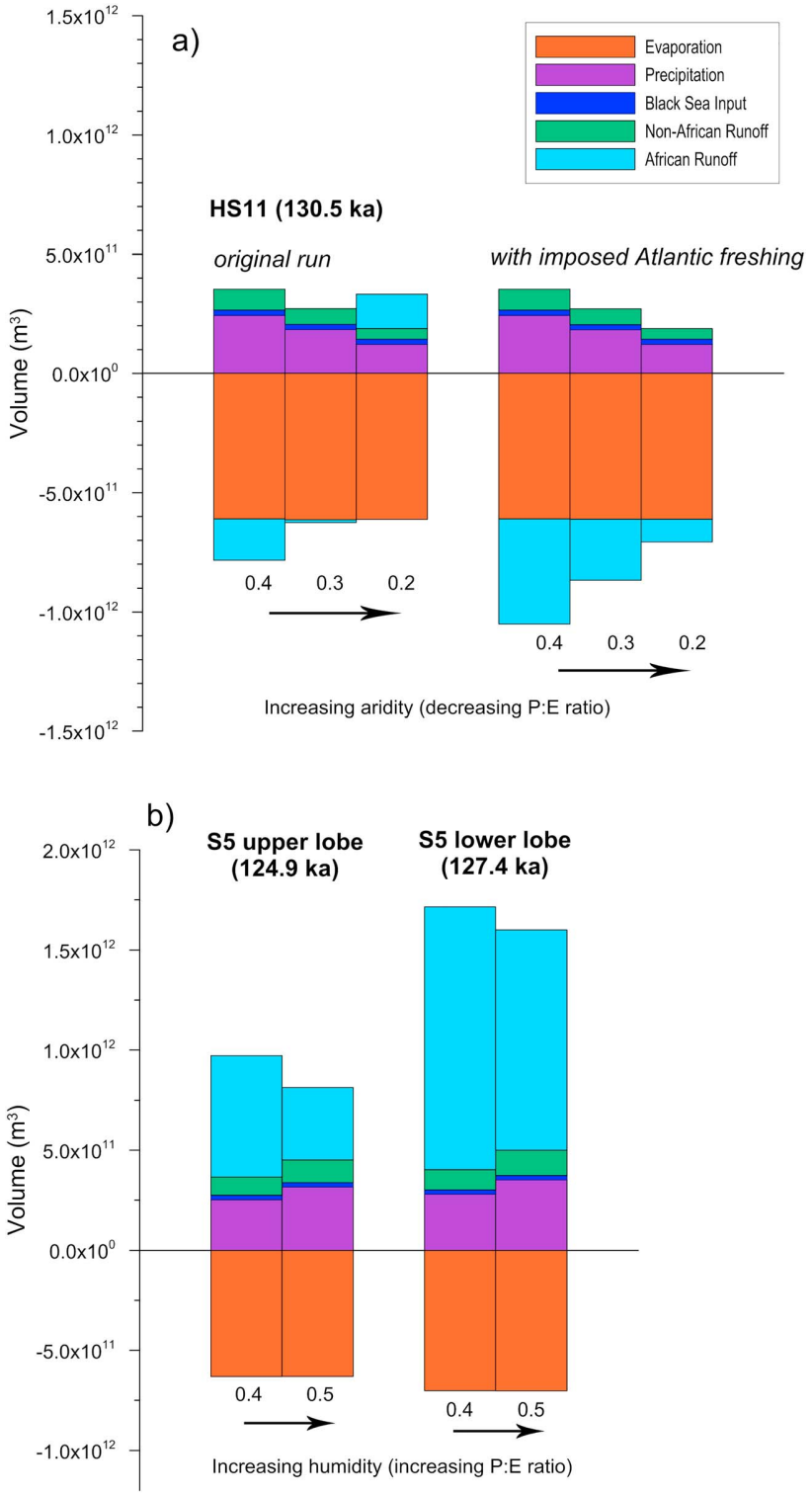

Figure 10. Modeled eastern Mediterranean hydrological balance during monsoon season for (a) HS11 (130.5 ka) and (b) S5 upper and lower lobes (124.8 and 127.3 ka). Different P:E ratios have been imposed on the Mediterranean box model to simulate different aridity/humidity conditions in the region. Volume fluxes for different components are shown as freshwater additions (positive) or removals (negative) to the basin system: evaporation (orange), precipitation (purple), Black Sea input (dark blue), non-African runoff (green), and African monsoonal runoff (blue).

model run (Figure 10a). This suggests that a climatic feature is captured in the data, which is not accounted for in the model, possibly an exceptionally evaporative period.

There is evidence of exceptionally arid conditions over North Africa and the Mediterranean during Heinrich stadials over the past 70 kyr (Collins et al., 2013; Combourieu Nebout et al., 2002; Niedermeyer et al., 2009; Torfstein et al., 2018). Pollen records from Southern Europe also suggest aridity during HS11, with drier, more open vegetation, and large expansion of interglacial vegetation occurring only after 130 ka (Figure 9g; e.g., Sánchez Goñi et al., 1999; Tzedakis et al., 2003; Brauer et al., 2007; Milner et al., 2012, 2016; Wulf et al., 2018). However, two independent Saharan dust proxies, one based on Ti/Al (Konijnendijk et al., 2014) and the other based on environmental magnetism ($IRM_{0.9T}@AF_{120mT}$; Larrasoaña, Roberts, Stoner, et al., 2003), as well as an aridity/humidity index for North Africa (Grant et al., 2017), imply a reduced influx of Saharan dust to the far eastern Mediterranean during HS11 (Figures 9h and 9i). This appears to suggest that HS11 was not as arid as is implied by our African monsoon runoff estimate. However, the weathering and erosion that produces Saharan dust requires, at least intermittently, humid conditions (Ehrmann et al., 2017; Kocurek, 1998). Therefore, a prolonged arid episode prior to HS11 may have depleted the Saharan dust available for aeolian transport (Kocurek, 1998). In particular, greater dust transport from Africa to the eastern Mediterranean resulting from increased cyclogenesis would be expected for the preceding glacial (Kuhlemann et al., 2008; Larrasoaña, Roberts, Stoner, et al., 2003). A reduced availability and/or transport of Saharan dust to the eastern Mediterranean would affect all of the aforementioned dust flux proxies, possibly masking an arid interval during HS11 in these records. Saharan lacustrine deposits potentially provide timing for North African humid intervals in a manner independent of Saharan dust (e.g., Drake et al., 2013; Geyh & Thiedig, 2008; Szabo et al., 1995), yet age uncertainties for these records are typically large and often span both S5 and HS11; therefore, unfortunately, such data cannot be used to resolve the issue.

Given that HS11 may have been a more arid period, we need to consider how this would affect the model results. The calculated runoff is essentially the difference in the Mediterranean evaporation-precipitation-runoff balance relative to that of the (pre-Aswan) present day. The model estimates the precipitation (over the sea), evaporation, and nonmonsoon runoff components, and the remainder is accounted for by a change in African monsoon runoff. Hence, an unquantified change in the past Mediterranean hydrological balance may not be fully accounted for in the model and may thus be falsely assigned as a change in monsoon runoff. As a result, negative monsoon runoff calculated during HS11 may reflect particularly enhanced aridity and a decreased precipitation to evaporation ratio (P:E) throughout the Mediterranean basin at this time. The P:E ratio in our box model was set to 0.4 ± 0.1 to allow variation from the present-day balance (0.4 ± 0.05; Mariotti et al., 2002). P:E was not set to change temporally through the study interval as this would require assumptions of past changes in aridity/humidity, and so far, quantitative paleoestimates of evaporation and precipitation over the Mediterranean remain elusive. A decrease in P:E to 0.29 avoids negative values for the median monsoon runoff volume from 131 to 129 ka in the model run without imposed HS11 Atlantic freshening (Figure 10a). However, for the additional model run with an imposed Atlantic freshening, P:E needs to be reduced to less than 0.2. This strongly suggests that the Atlantic freshening during HS11 imposed in this run has been overestimated.

On the other hand, the S5 interval is associated with an African humid period. This might be accompanied by greater humidity over the Mediterranean (greater P:E). For an increase in the box model P:E to 0.5 (from 0.4), the median African monsoon runoff is reduced to a maximum of $\sim 1.1 \times 10^{12}$ m^3 for the lower lobe of S5 (monsoonal intensification of ~7.3, down from ~8.8), and $\sim 3.6 \times 10^{11}$ m^3 for the upper lobe (monsoonal intensification of ~2.4, down from ~4; Figure 10b). While these are well within the 68% probability envelope of our calculated African monsoon runoff (Figure 9c), this indicates how quantification of past changes in the hydrological balance of the Mediterranean would help refine our estimates.

8. Conclusions

We have deconvolved Mediterranean $\delta^{18}O_{pf}$ to calculate African monsoon runoff history over the period of deposition of sapropel S5 (~128.3–121.5 ka). This was achieved using a box model of the Mediterranean, which was constrained with existing records of sea level and SST. Our calculations provide the first quantitative time series estimate of the extent of North African monsoon intensification, which is widely accepted as a major cause of eastern Mediterranean sapropels. Our estimated African monsoon runoff volume

suggests that large increases in freshwater runoff into the eastern Mediterranean (up to ~8.8 times the modern pre-Aswan Nile discharge) are required to account for the $\delta^{18}O_{ruber}$ signals during sapropel S5 deposition, while remaining consistent with the $\delta^{18}O$ profiles of other planktic foraminifera species. The method also indicates that SST increase ($\leq$5.7 °C) via a *temperature concentration* effect accounts for a large part of the *sapropel imprint* on $\delta^{18}O_{ruber}$ and cannot be ignored. Our experiments suggest that ΔT, the difference between the $U^{K'}_{37}$ (+4 °C) and the Δ_{47}-*G. ruber* (w) summer temperature reconstructions, reflects the temperature concentration effect and hence the extent of freshwater-induced and temperature-enforced stratification in the SML during the S5 interval.

The calculated increase in African monsoon runoff first exceeds modern pre-Aswan values at 128.5 ka, only ~200 years before the onset of S5. Previously published data suggest an enhanced stratification in the eastern Mediterranean before S5, likely related to Termination II sea level rise or HS11 Atlantic freshening, which may have preconditioned the basin for the rapid onset of sapropel deposition following the increase in monsoon freshwater influx. Two main intervals of increased African runoff are identified over the interval of S5 deposition, the lower lobe (128.5–126.5 ka; peak median runoff volume of ~1.3×10^{12} m^3/year), and the upper lobe (125.7–122.8 ka; runoff volume ~$2.4–6.1 \times 10^{11}$ m^3/year). In between these two intervals, runoff decreases to volumes similar to the pre-Aswan modern values. Improvements in constraining past variations in the Mediterranean P:E balance would refine our median estimates of African monsoon runoff, although such differences remain well within our 68% probability intervals.

The method developed here provides a more detailed insight into the hydrological conditions in the eastern Mediterranean (and North Africa) during the last interglacial, and there is potential to apply the method to other intervals of sapropel deposition. Furthermore, the ability to deconvolve $\delta^{18}O_{ruber}$ and isolate the freshwater component during sapropel events is a step towards reconstructing sea levels over sapropel events using the Mediterranean marginal-basin sea-level method (Rohling et al., 2014).

Acknowledgments

We dedicate this study to the memory of Bob Thunell. One of us (E. J. R.) was inspired in the late 1980s to early 1990s by Bob's work in the Mediterranean and Red Sea. Through the years, many new concepts and ideas were refined through discussions with Bob, notably during AGU Fall Meetings. This includes aspects of the approach followed in this study. We would like to thank two anonymous reviewers, Larry Peterson (Guest Associate Editor) and Ellen Thomas (Editor) for their constructive comments and recommendations. This work was supported by Australian Research Council (ARC) Australian Laureate Fellowship FL120100050 (E. J. R.) and Discovery Early Career Researcher Award DE190100042 (K. M. G.). G. M. acknowledges support from the University of Vigo program to attract excellent research talent and a generous start-up package. We thank the Ocean Discovery Program (ODP), which provided the samples, and the Australia-New Zealand IODP Consortium (ANZIC), which provided Legacy/Special Analytical Funding for this study (LE140100047 and LE160100067; L. R. S. and K. M. G.). New data presented here are available at https://doi.org/10.1594/PANGAEA.901419

References

Al Faitouri, M., & Sanford, W. E. (2015). Stable and radio-isotope analysis to determine recharge timing and paleoclimate of sandstone aquifers in central and southeast Libya. *Hydrogeology Journal*, *23*(4), 707–717. https://doi.org/10.1007/s10040-015-1232-7

Bar-Matthews, M., Ayalon, A., & Kaufman, A. (2000). Timing and hydrological conditions of Sapropel events in the Eastern Mediterranean, as evident from speleothems, Soreq cave, Israel. *Chemical Geology*, *169*(1–2), 145–156. https://doi.org/10.1016/S0009-2541(99)00232-6

Berger, A., & Loutre, M. F. (1991). Insolation values for the climate of the last 10 million years. *Quaternary Science Reviews*, *10*(4), 297–317. https://doi.org/10.1016/0277-3791(91)90033-Q

Beuning, K. R. M., Kelts, K., Russell, J., & Wolfe, B. B. (2002). Reassessment of Lake Victoria–Upper Nile River paleohydrology from oxygen isotope records of lake-sediment cellulose. *Geology*, *30*(6), 559–562. https://doi.org/10.1130/0091-7613(2002)030 < 0559:ROLVUN>2.0.CO;2

Brauer, A., Allen, J. R. M., Mingram, J., Dulski, P., Wulf, S., & Huntley, B. (2007). Evidence for last interglacial chronology and environmental change from Southern Europe. *Proceedings of the National Academy of Sciences of the United States of America*, *104*(2), 450–455. https://doi.org/10.1073/pnas.0603321104

Bryden, H. L., & Kinder, T. H. (1991). Steady two-layer exchange through the Strait of Gibraltar, *Deep Sea Research Part A. Oceanographic Research Papers*, *38*, S445–S463. https://doi.org/10.1016/S0198-0149(12)80020-3

Calvert, S. E., Nielsen, B., & Fontugne, M. R. (1992). Evidence from nitrogen isotope ratios for enhanced productivity during formation of eastern Mediterranean sapropels. *Nature*, *359*(6392), 223–225. https://doi.org/10.1038/359223a0

Cane, T., Rohling, E. J., Kemp, A. E. S., Cooke, S., & Pearce, R. B. (2002). High-resolution stratigraphic framework for Mediterranean sapropel S5: Defining temporal relationships between records of Eemian climate variability. *Palaeogeography, Palaeoclimatology, Palaeoecology*, *183*(1–2), 87–101. https://doi.org/10.1016/S0031-0182(01)00461-8

Carter, D. B. (1956). The water balance of the Mediterranean and Black Seas. *Publications in Climatology*, *9*(3), 127–174.

Castañeda, I. S., Schefuß, E., Pätzold, J., Sinninghe Damsté, J. S., Weldeab, S., & Schouten, S. (2010). Millennial-scale sea surface temperature changes in the eastern Mediterranean (Nile River Delta region) over the last 27,000 years. *Paleoceanography*, *25*, PA1208. https://doi.org/10.1029/2009PA001740

Collins, J. A., Govin, A., Mulitza, S., Heslop, D., Zabel, M., Hartmann, J., et al. (2013). Abrupt shifts of the Sahara–Sahel boundary during Heinrich stadials. *Climate of the Past*, *9*(3), 1181–1191. https://doi.org/10.5194/cp-9-1181-2013

Combourieu Nebout, N., Turon, J. L., Zahn, R., Capotondi, L., Londeix, L., & Pahnke, K. (2002). Enhanced aridity and atmospheric high-pressure stability over the western Mediterranean during the North Atlantic cold events of the past 50 k.y. *Geology*, *30*(10), 863–866. https://doi.org/10.1130/0091-7613(2002)030 < 0863:EAAAHP>2.0.CO;2

Coulthard, T. J., Ramirez, J. A., Barton, N., Rogerson, M., & Brücher, T. (2013). Were rivers flowing across the Sahara during the Last Interglacial? Implications for human migration through Africa. *PLoS ONE*, *8*(9), e74834. https://doi.org/10.1371/journal.pone.0074834

D'Ortenzio, F., Iudicone, D., de Boyer Montegut, C., Testor, P., Antoine, D., Marullo, S., et al. (2005). Seasonal variability of the mixed layer depth in the Mediterranean Sea as derived from in situ profiles. *Geophysical Research Letters*, *32*, L12605. https://doi.org/10.1029/2005GL022463

Dirksen, J. P., Hennekam, R., Geerken, E., & Reichart, G. (2019). A novel approach using time-depth distortions to assess multicentennial variability in deep-sea oxygen deficiency in the eastern Mediterranean Sea during Sapropel S5. *Paleoceanography and Paleoclimatology*, *34*, 774–786. https://doi.org/10.1029/2018PA003458

Drake, N. A., Breeze, P., & Parker, A. (2013). Palaeoclimate in the Saharan and Arabian Deserts during the Middle Palaeolithic and the potential for hominin dispersals. *Quaternary International*, *300*, 48–61. https://doi.org/10.1016/J.QUAINT.2012.12.018

Ehrmann, W., Schmiedl, G., Beuscher, S., & Krüger, S. (2017). Intensity of African humid periods estimated from Saharan dust fluxes. *PLOS ONE*, *12*(1), e0170989. https://doi.org/10.1371/journal.pone.0170989

Elderfield, H., Ferretti, P., Greaves, M., Crowhurst, S., McCave, I. N., Hodell, D., & Piotrowski, A. M. (2012). Evolution of ocean temperature and ice volume through the Mid-Pleistocene climate transition. *Science*, *337*(6095), 704–709. https://doi.org/10.1126/science.1221294

Emeis, K.-C., Sakamoto, T., Wehausen, R., & Brumsack, H.-J. (2000). The sapropel record of the eastern Mediterranean Sea—Results of Ocean Drilling Program Leg 160. *Palaeogeography, Palaeoclimatology, Palaeoecology*, *158*(3–4), 371–395. https://doi.org/10.1016/S0031-0182(00)00059-6

Emeis, K. C., Schulz, H., Struck, U., Rossignol-Strick, M., Erlenkeuser, H., Howell, M. W., et al. (2003). Eastern Mediterranean surface water temperatures and $\delta^{18}O$ composition during deposition of sapropels in the late Quaternary. *Paleoceanography*, *18*(1), 1005. https://doi.org/10.1029/2000PA000617

Emeis, K.-C., Struck, U., Schulz, H.-M., Rosenberg, R., Bernasconi, S., Erlenkeuser, H., et al. (2000). Temperature and salinity variations of Mediterranean Sea surface waters over the last 16,000 years from records of planktonic stable oxygen isotopes and alkenone unsaturation ratios. *Palaeogeography, Palaeoclimatology, Palaeoecology*, *158*(3–4), 259–280. https://doi.org/10.1016/S0031-0182(00)00053-5

Gasse, F. (2000). Hydrological changes in the African tropics since the Last Glacial Maximum. *Quaternary Science Reviews*, *19*(1-5), 189–211 . https://doi.org/10.1016/S0277-3791(99)00061-X

Garrett, C., Outerbridge, R., & Thompson, K. (1993). Interannual variability in Meterrancan heat and buoyancy fluxes. *Journal of Climate*, *6*(5), 900–910. https://doi.org/10.1175/1520-0442(1993)006 < 0900:IVIMHA>2.0.CO;2

Geyh, M. A., & Thiedig, F. (2008). The Middle Pleistocene Al Mahrúqah Formation in the Murzuq Basin, northern Sahara, Libya evidence for orbitally-forced humid episodes during the last 500,000 years. *Palaeogeography, Palaeoclimatology, Palaeoecology*, *257*(1–2), 1–21. https://doi.org/10.1016/J.PALAEO.2007.07.001

Goudeau, M.-L. S., Grauel, A.-L., Tessarolo, C., Leider, A., Chen, L., Bernasconi, S. M., et al. (2014). The glacial–interglacial transition and Holocene environmental changes in sediments from the Gulf of Taranto, central Mediterranean. *Marine Geology*, *348*, 88–102. https://doi.org/10.1016/j.margeo.2013.12.003

Grant, K. M., Grimm, R., Mikolajewicz, U., Marino, G., Ziegler, M., & Rohling, E. J. (2016). The timing of Mediterranean sapropel deposition relative to insolation, sea-level and African monsoon changes. *Quaternary Science Reviews*, *140*, 125–141. https://doi.org/10.1016/j.quascirev.2016.03.026

Grant, K. M., Rohling, E. J., Bar-Matthews, M., Ayalon, A., Medina-Elizalde, M., Ramsey, C. B., et al. (2012). Rapid coupling between ice volume and polar temperature over the past 150,000 years. *Nature*, *491*(7426), 744–747. https://doi.org/10.1038/nature11593

Grant, K. M., Rohling, E. J., Westerhold, T., Zabel, M., Heslop, D., Konijnendijk, T., & Lourens, L. (2017). A 3 million year index for North African humidity/aridity and the implication of potential pan-African Humid periods. *Quaternary Science Reviews*, *171*, 100–118. https://doi.org/10.1016/j.quascirev.2017.07.005

Grelaud, M., Marino, G., Ziveri, P., & Rohling, E. J. (2012). Abrupt shoaling of the nutricline in response to massive freshwater flooding at the onset of the last interglacial sapropel event. *Paleoceanography*, *27*, PA3208. https://doi.org/10.1029/2012PA002288

Grimm, R., Maier-Reimer, E., Mikolajewicz, U., Schmiedl, G., Müller-Navarra, K., Adloff, F., et al. (2015). Late glacial initiation of Holocene eastern Mediterranean sapropel formation. *Nature Communications*, *6*(1), 7099. https://doi.org/10.1038/ncomms8099

van Helmond, N. A. G. M., Hennekam, R., Donders, T. H., Bunnik, F. P. M., de Lange, G. J., Brinkhuis, H., & Sangiorgi, F. (2015). Marine productivity leads organic matter preservation in sapropel S1: Palynological evidence from a core east of the Nile River outflow. *Quaternary Science Reviews*, *108*, 130–138. https://doi.org/10.1016/j.quascirev.2014.11.014

Hennekam, R., Jilbert, T., Schnetger, B., & de Lange, G. J. (2014). Solar forcing of Nile discharge and sapropel S1 formation in the early to middle Holocene eastern Mediterranean. *Paleoceanography*, *29*, 343–356. https://doi.org/10.1002/2013PA002553

Hibbert, F. D., Rohling, E. J., Dutton, A., Williams, F. H., Chutcharavan, P. M., Zhao, C., & Tamisiea, M. E. (2016). Coral indicators of past sea-level change: A global repository of U-series dated benchmarks. *Quaternary Science Reviews*, *145*, 1–56. https://doi.org/10.1016/j.quascirev.2016.04.019

Hilgen, F. J. (1991). Astronomical calibration of Gauss to Matuyama sapropels in the Mediterranean and implication for the Geomagnetic Polarity Time Scale. *Earth and Planetary Science Letters*, *104*(2-4), 226–244. https://doi.org/10.1016/0012-821X(91)90206-W

Hoelzmann, P. (2000). Precipitation estimates for the eastern Saharan palaeomonsoon based on a water balance model of the West Nubian Palaeolake Basin. *Global and Planetary Change*, *26*(1–3), 105–120. https://doi.org/10.1016/S0921-8181(00)00038-2

Incarbona, A., Sprovieri, M., Lirer, F., & Sprovieri, R. (2011). Surface and deep water conditions in the Sicily channel (central Mediterranean) at the time of sapropel S5 deposition. *Palaeogeography, Palaeoclimatology, Palaeoecology*, *306*(3–4), 243–248. https://doi.org/10.1016/j.palaeo.2011.04.030

Irvalı, N., Ninnemann, U. S., Galaasen, E. V., Rosenthal, Y., Kroon, D., Oppo, D. W., et al. (2012). Rapid switches in subpolar North Atlantic hydrography and climate during the Last Interglacial (MIS 5e). *Paleoceanography*, *27*, PA2207. https://doi.org/10.1029/2011PA002244

Jiménez-Amat, P., & Zahn, R. (2015). Offset timing of climate oscillations during the last two glacial-interglacial transitions connected with large-scale freshwater perturbation. *Paleoceanography*, *30*, 768–788. https://doi.org/10.1002/2014PA002710

Jorissen, F. J. (1999). Benthic foraminiferal successions across Late Quaternary Mediterranean sapropels. *Marine Geology*, *153*(1–4), 91–101 . https://doi.org/10.1016/S0025-3227(98)00088-7

Kocurek, G. (1998). Aeolian system response to external forcing factors—A sequence stratigraphic view of the Saharan region. In A. S. Alsharhan, et al. (Eds.), *Quaternary Deserts and Climatic Change*, (pp. 327–337). Balkema Rotterdam.

Konijnendijk, T. Y. M., Ziegler, M., & Lourens, L. J. (2014). Chronological constraints on Pleistocene sapropel depositions from high-resolution geochemical records of ODP Sites 967 and 968. *Newsletters on Stratigraphy*, *47*(3), 263–282. https://doi.org/10.1127/0078-0421/2014/0047

Koopmans, M. P., Köster, J., Van Kaam-Peters, H. M. E., Kenig, F., Schouten, S., Hartgers, W. A., et al. (1996). Diagenetic and catagenetic products of isorenieratene: Molecular indicators for photic zone anoxia. *Geochimica et Cosmochimica Acta*, *60*(22), 4467–4496. https://doi.org/10.1016/S0016-7037(96)00238-4

Kopp, R. E., Simons, F. J., Mitrovica, J. X., Maloof, A. C., & Oppenheimer, M. (2009). Probabilistic assessment of sea level during the last interglacial stage. *Nature*, *462*(7275), 863–867. https://doi.org/10.1038/nature08686

Kotthoff, U., Pross, J., Müller, U. C., Peyron, O., Schmiedl, G., Schulz, H., & Bordon, A. (2008). Climate dynamics in the borderlands of the Aegean Sea during formation of sapropel S1 deduced from a marine pollen record. *Quaternary Science Reviews*, *27*(7–8), 832–845. https://doi.org/10.1016/J.QUASCIREV.2007.12.001

Kuhlemann, J., Rohling, E. J., Krumrei, I., Kubik, P., Ivy-Ochs, S., & Kucera, M. (2008). Regional synthesis of Mediterranean atmospheric circulation during the Last Glacial Maximum. *Science*, *321*(5894), 1338–1340. https://doi.org/10.1126/science.1157638

Kutzbach, J. E., Chen, G., Cheng, H., Edwards, R. L., & Liu, Z. (2014). Potential role of winter rainfall in explaining increased moisture in the Mediterranean and Middle East during periods of maximum orbitally-forced insolation seasonality. *Climate Dynamics*, *42*(3-4), 1079–1095. https://doi.org/10.1007/s00382-013-1692-1

Lane-Serff, G. F., Rohling, E. J., Bryden, H. L., & Charnock, H. (1997). Postglacial connection of the Black Sea to the Mediterranean and its relation to the timing of sapropel formation. *Paleoceanography*, *12*(2), 169–174. https://doi.org/10.1029/96PA03934

de Lange, G. J., & ten Haven, H. L. (1983). Recent sapropel formation in the eastern Mediterranean. *Nature*, *305*(5937), 797–798. https://doi.org/10.1038/305797a0

Larrasoaña, J. C., Roberts, A. P., & Rohling, E. J. (2013). Dynamics of green Sahara periods and their role in Hominin evolution. *Plos One*, *8*(10). https://doi.org/10.1371/journal.pone.0076514.g001

Larrasoaña, J. C., Roberts, A. P., Rohling, E. J., Winklhofer, M., & Wehausen, R. (2003). Three million years of monsoon variability over the northern Sahara. *Climate Dynamics*, *21*(7–8), 689–698. https://doi.org/10.1007/s00382-003-0355-z

Larrasoaña, J. C., Roberts, A. P., Stoner, J. S., Richter, C., & Wehausen, R. (2003). A new proxy for bottom-water ventilation in the eastern Mediterranean based on diagenetically controlled magnetic properties of sapropel-bearing sediments. *Palaeogeography, Palaeoclimatology, Palaeoecology*, *190*, 221–242. https://doi.org/10.1016/S0031-0182(02)00607-7

Leider, A., Hinrichs, K.-U., Mollenhauer, G., & Versteegh, G. J. M. (2010). Core-top calibration of the lipid-based U37K′ and TEX86 temperature proxies on the southern Italian shelf (SW Adriatic Sea, Gulf of Taranto). *Earth and Planetary Science Letters*, *300*(1-2), 112–124. https://doi.org/10.1016/j.epsl.2010.09.042

Locarnini, R. A., Mishonov, A. V., Antonov, J. I., Boyer, T. P., Garcia, H. E., Baranova, O. K., et al. (2010). World Ocean Atlas 2009, Volume 1: Temperature. Edited by S. Levitus. Washington, D.C.: NOAA Atlas NESDIS 68, U.S. Government Printing Office.

Lourens, L. J., Hilgen, F. J., Raffi, I., & Vergnaud-Grazzini, C. (1996). Early Pleistocene chronology of the Vrica Section (Calabria, Italy). *Paleoceanography*, *11*(6), 797–812. https://doi.org/10.1029/96PA02691

Lourens, L. J., Wehausen, R., & Brumsack, H. J. (2001). Geological constraints on tidal dissipation and dynamical ellipticity of the Earth over the past three million years. *Nature*, *409*(6823), 1029–1033. https://doi.org/10.1038/35059062

Ludwig, W., Dumont, E., Meybeck, M., & Heussner, S. (2009). River discharges of water and nutrients to the Mediterranean and Black Sea: Major drivers for ecosystem changes during past and future decades? *Progress in Oceanography*, *80*(3–4), 199–217. https://doi.org/10.1016/J.POCEAN.2009.02.001

Marino, G., Rohling, E. J., Rijpstra, W. I. C., Sangiorgi, F., Schouten, S., & Damsté, J. S. S. (2007). Aegean Sea as driver of hydrographic and ecological changes in the eastern Mediterranean. *Geology*, *35*(8), 675–678. https://doi.org/10.1130/g23831a.1

Marino, G., Rohling, E. J., Rodríguez-Sanz, L., Grant, K. M., Heslop, D., Roberts, A. P., et al. (2015). Bipolar seesaw control on last interglacial sea level. *Nature*, *522*(7555), 197–201. https://doi.org/10.1038/nature14499

Marino, G., Rohling, E. J., Sangiorgi, F., Hayes, A., Casford, J. L., Lotter, A. F., et al. (2009). Early and middle Holocene in the Aegean Sea: Interplay between high and low latitude climate variability. *Quaternary Science Reviews*, *28*(27–28), 3246–3262. https://doi.org/10.1016/j.quascirev.2009.08.011

Mariotti, A., Struglia, M. V., Zeng, N., & Lau, K.-M. (2002). The hydrological cycle in the Mediterranean region and implications for the water budget of the Mediterranean Sea. *Journal of Climate*, *15*(13), 1674–1690. https://doi.org/10.1175/1520-0442(2002)015 < 1674:THCITM>2.0.CO;2

Martrat, B., Jimenez-Amat, P., Zahn, R., & Grimalt, J. O. (2014). Similarities and dissimilarities between the last two deglaciations and interglaciations in the North Atlantic region. *Quaternary Science Reviews*, *99*, 122–134. https://doi.org/10.1016/j.quascirev.2014.06.016

Matthiesen, S., & Haines, K. (2003). A hydraulic box model study of the Mediterranean response to postglacial sea-level rise. *Paleoceanography*, *18*(4), 1084. https://doi.org/10.1029/2003PA000880

McKenzie, J. A. (1993). Pluvial conditions in the eastern Sahara following the penultimate deglaciation: Implications for changes in atmospheric circulation patterns with global warming. *Palaeogeography, Palaeoclimatology, Palaeoecology*, *103*(1–2), 95–105. https://doi.org/10.1016/0031-0182(93)90054-M

Milner, A. M., Collier, R. E. L., Roucoux, K. H., Müller, U. C., Pross, J., Kalaitzidis, S., et al. (2012). Enhanced seasonality of precipitation in the Mediterranean during the early part of the Last Interglacial. *Geology*, *40*(10), 919–922. https://doi.org/10.1130/G33204.1

Milner, A. M., Roucoux, K. H., Collier, R. E. L., Müller, U. C., Pross, J., & Tzedakis, P. C. (2016). Vegetation responses to abrupt climatic changes during the Last Interglacial Complex (Marine Isotope Stage 5) at Tenaghi Philippon, NE Greece. *Quaternary Science Reviews*, *154*, 169–181. https://doi.org/10.1016/j.quascirev.2016.10.016

Myers, P. G., Haines, K., & Rohling, E. J. (1998). Modeling the paleocirculation of the Mediterranean: The Last Glacial Maximum and the Holocene with emphasis on the formation of sapropel S 1. *Paleoceanography*, *13*(6), 586–606. https://doi.org/10.1029/98PA02736

Niedermeyer, E. M., Prange, M., Mulitza, S., Mollenhauer, G., Schefuß, E., & Schulz, M. (2009). Extratropical forcing of Sahel aridity during Heinrich stadials. *Geophysical Research Letters*, *36*, L20707. https://doi.org/10.1029/2009GL039687

Nykjaer, L. (2009). Mediterranean Sea surface warming 1985–2006. *Climate Research*, *39*, 11–17. https://doi.org/10.3354/cr00794

Olausson, E. (1991). A post-Cromerian rise in sea level, in International conference on the role of the polar regions in global change: Proceedings. Volume 2, 496–498.

Osborne, A. H., Marino, G., Vance, D., & Rohling, E. J. (2010). Eastern Mediterranean surface water Nd during Eemian sapropel S5: Monitoring northerly (mid-latitude) versus southerly (sub-tropical) freshwater contributions. *Quaternary Science Reviews*, *29*(19–20), 2473–2483. https://doi.org/10.1016/j.quascirev.2010.05.015

Osborne, A. H., Vance, D., Rohling, E. J., Barton, N., Rogerson, M., & Fello, N. (2008). A humid corridor across the Sahara for the migration of early modern humans out of Africa 120,000 years ago. *Proceedings of the National Academy of Sciences*, *105*(43), 16444–16447. https://doi.org/10.1073/pnas.0804472105

Pachur, H.-J. (2001). Holozäne Klimawechsel in den nördlichen Subtropen. *Nova Acta Leopoldina NF88*, *331*, 109–131.

Paillou, P., Schuster, M., Tooth, S., Farr, T., Rosenqvist, A., Lopez, S., & Malezieux, J.-M. (2009). Mapping of a major paleodrainage system in eastern Libya using orbital imaging radar: The Kufrah River. *Earth and Planetary Science Letters*, *277*(3–4), 327–333. https://doi.org/10.1016/j.epsl.2008.10.029

Passier, H. F., Bosch, H.-J., Nijenhuis, I. A., Lourens, L. J., Böttcher, M. E., Leenders, A., et al. (1999). Sulphidic Mediterranean surface waters during Pliocene sapropel formation. *Nature*, *397*(6715), 146–149. https://doi.org/10.1038/16441

Pinardi, N., Zavatarelli, M., Adani, M., Coppini, G., Fratianni, C., Oddo, P., et al. (2015). Mediterranean Sea large-scale low-frequency ocean variability and water mass formation rates from 1987 to 2007: A retrospective analysis. *Progress in Oceanography*, *132*, 318–332. https://doi.org/10.1016/j.pocean.2013.11.003

Repeta, D. J., Simpson, D. J., Jorgensen, B. B., & Jannasch, H. W. (1989). Evidence for anoxygenic photosynthesis from the distribution of bacterio-chlorophylls in the Black Sea. *Nature*, *342*(6245), 69–72. https://doi.org/10.1038/342069a0

Revel, M., Ducassou, E., Grousset, F. E., Bernasconi, S. M., Migeon, S., Revillon, S., et al. (2010). 100,000 Years of African monsoon variability recorded in sediments of the Nile margin. *Quaternary Science Reviews*, *29*(11–12), 1342–1362. https://doi.org/10.1016/j.quascirev.2010.02.006

Rodrigues, D., Abell, P. I., & Kröpelin, S. (2000). Seasonality in the early Holocene climate of Northwest Sudan: Interpretation of Etheria elliptica shell isotopic data. *Global and Planetary Change*, *26*(1–3), 181–187. https://doi.org/10.1016/S0921-8181(00)00043-6

Rodríguez-Sanz, L., Bernasconi, S. M., Marino, G., Heslop, D., Müller, I. A., Fernandez, A., et al. (2017). Penultimate deglacial warming across the Mediterranean Sea revealed by clumped isotopes in foraminifera. *Scientific Reports*, *7*(1), 16572. https://doi.org/10.1038/s41598-017-16528-6

Rohling, E. J. (1991). Shoaling of the Eastern Mediterranean Pycnocline due to reduction of excess evaporation: Implications for sapropel formation. *Paleoceanography*, *6*(6), 747–753. https://doi.org/10.1029/91PA02455

Rohling, E. J. (1994). Review and new aspects concerning the formation of eastern Mediterranean sapropels. *Marine Geology*, *122*(1–2), 1–28. https://doi.org/10.1016/0025-3227(94)90202-X

Rohling, E. J. (1999). Environmental control on Mediterranean salinity and $\delta^{18}O$. *Paleoceanography*, *14*(6), 706–715. https://doi.org/10.1029/1999PA900042

Rohling, E. J., Cane, T. R., Cooke, S., Sprovieri, M., Bouloubassi, I., Emeis, K. C., et al. (2002). African monsoon variability during the previous interglacial maximum. *Earth and Planetary Science Letters*, *202*(1), 61–75. https://doi.org/10.1016/S0012-821X(02)00775-6

Rohling, E. J., Foster, G. L., Grant, K. M., Marino, G., Roberts, A. P., Tamisiea, M. E., & Williams, F. (2014). Sea-level and deep-sea-temperature variability over the past 5.3 million years. *Nature*, *508*(7497), 477–482. https://doi.org/10.1038/nature13230

Rohling, E. J., & Gieskes, W. W. C. (1989). Late Quaternary changes in Mediterranean intermediate water density and formation rate. *Paleoceanography*, *4*(5), 531–545. https://doi.org/10.1029/PA004i005p00531

Rohling, E. J., Grant, K., Hemleben, C., Siddall, M., Hoogakker, B. A. A., Bolshaw, M., & Kucera, M. (2008). High rates of sea-level rise during the last interglacial period. *Nature Geoscience*, *1*(1), 38–42. https://doi.org/10.1038/ngeo.2007.28

Rohling, E. J., Hopmans, E. C., & Sinninghe Damsté, J. S. (2006). Water column dynamics during the last interglacial anoxic event in the Mediterranean (sapropel S5). *Paleoceanography*, *21*, PA2018. https://doi.org/10.1029/2005pa001237

Rohling, E. J., Marino, G., & Grant, K. M. (2015). Mediterranean climate and oceanography, and the periodic development of anoxic events (sapropels). *Earth-Science Reviews*, *143*, 62–97. https://doi.org/10.1016/j.earscirev.2015.01.008

Rohling, E. J., Sprovieri, M., Cane, T., Casford, J. S. L., Cooke, S., Bouloubassi, I., et al. (2004). Reconstructing past planktic foraminiferal habitats using stable isotope data: A case history for Mediterranean sapropel S5. *Marine Micropaleontology*, *50*(1–2), 89–123. https://doi.org/10.1016/S0377-8398(03)00068-9

Rossignol-Strick, M. (1985). Mediterranean Quaternary sapropels, an immediate response of the African monsoon to variation of insolation. *Palaeogeography, Palaeoclimatology, Palaeoecology*, *49*(3–4), 237–263. https://doi.org/10.1016/0031-0182(85)90056-2

Rossignol-Strick, M., Nesteroff, W., Olive, P., & Vergnaud-Grazzini, C. (1982). After the deluge: Mediterranean stagnation and sapropel formation. *Nature*. Nature Publishing Group, *295*(5845), 105–110. https://doi.org/10.1038/295105a0

Salonen, J. S., Helmens, K. F., Brendryen, J., Kuosmanen, N., Väliranta, M., Goring, S., et al. (2018). Abrupt high-latitude climate events and decoupled seasonal trends during the Eemian. *Nature Communications*, *9*(1), 2851. https://doi.org/10.1038/s41467-018-05314-1

Sánchez Goñi, M. F., Eynaud, F., Turon, J. L., & Shackleton, N. J. (1999). High resolution palynological record off the Iberian margin: Direct land-sea correlation for the Last Interglacial complex. *Earth and Planetary Science Letters*, *171*(1), 123–137. https://doi.org/10.1016/S0012-821X(99)00141-7

Schiebel, R., & Hemleben, C. (2017). *Planktic foraminifers in the Modern Ocean*. Berlin, Heidelberg: Springer Berlin Heidelberg. https://doi.org/10.1007/978-3-662-50297-6

Schink, D. R. (1967). Budget for dissolved silica in the Mediterranean Sea. *Geochimica et Cosmochimica Acta*, *31*(6), 987–999. https://doi.org/10.1016/0016-7037(67)90075-0

Schlitzer, R. (2016) 'Ocean Data View'

Scrivner, A. E., Vance, D., & Rohling, E. J. (2004). New neodymium isotope data quantify Nile involvement in Mediterranean anoxic episodes. *Geology*, *32*(7), 565. https://doi.org/10.1130/g20419.1

Shipboard Scientific Party (1996a). Site 967, in Emeis, K.-C. et al. (eds) Proceedings of the Ocean Drilling Program, 160 Initial Reports. Ocean Drilling Program, College Station, TX, 155–213. doi: https://doi.org/10.2973/odp.proc.ir.160.108.1996

Shipboard Scientific Party (1996b). Site 971, in Emeis, K.-C. et al. (eds) Proceedings of the Ocean Drilling Program, 160 Initial Reports. Ocean Drilling Program, College Station, TX, 215–287. doi: https://doi.org/10.2973/odp.proc.ir.160.112.1996

Sierro, F. J., Hodell, D. A., Curtis, J. H., Flores, J. A., Reguera, I., Colmenero-Hidalgo, E., et al. (2005). Impact of iceberg melting on Mediterranean thermohaline circulation during Heinrich events. *Paleoceanography*, *20*, PA2019. https://doi.org/10.1029/2004PA001051

Skinner, L. C., & Shackleton, N. J. (2006). Deconstructing Terminations I and II: Revisiting the glacioeustatic paradigm based on deep-water temperature estimates. *Quaternary Science Reviews*, *25*(23–24), 3312–3321. https://doi.org/10.1016/J.QUASCIREV.2006.07.005

Sonntag, C., Klitzsch, E., Löhnert, E. P., El-Shazly, E. M., Münnich, K., et al. (1979). Palaeoclimatic information from deuterium and oxygen-18 and carbon-14 dated North Saharian groundwaters. Groundwater formation in the past. In *Isotope Hydrology 1978 (Proceedings Series, Vol. II, 569–581)*. Vienna: International Atomic Energy Agency.

Stanev, E. V., Friedrich, H. J., & Botev, S. V. (1989). On the seasonal response of intermediate and deep water to surface forcing in the Mediterranean Sea. *Oceanologica Acta*, *12*(2), 141–149.

Struglia, M. V., Mariotti, A., Filograsso, A., Struglia, M. V., Mariotti, A., & Filograsso, A. (2004). River discharge into the Mediterranean Sea: Climatology and aspects of the observed variability. *Journal of Climate*, *17*(24), 4740–4751. https://doi.org/10.1175/JCLI-3225.1

Swingedouw, D., Rodehacke, C. B., Behrens, E., Menary, M., Olsen, S. M., Gao, Y., et al. (2013). Decadal fingerprints of freshwater discharge around Greenland in a multi-model ensemble. *Climate Dynamics*, *41*(3–4), 695–720. https://doi.org/10.1007/s00382-012-1479-9

Szabo, B. J., Haynes, C. V., & Maxwell, T. A. (1995). Ages of Quaternary pluvial episodes determined by uranium-series and radiocarbon dating of lacustrine deposits of Eastern Sahara. *Palaeogeography, Palaeoclimatology, Palaeoecology*, *113*(2–4), 227–242. https://doi.org/10.1016/0031-0182(95)00052-N

Tang, C. M., & Stott, L. D. (1993). Seasonal salinity changes during Mediterranean sapropel deposition 9000 years B.P.: Evidence from isotopic analyses of individual planktonic foraminifera. *Paleoceanography*, *8*(4), 473–493. https://doi.org/10.1029/93PA01319

Thirumalai, K., Quinn, T. M., & Marino, G. (2016). Constraining past seawater $\delta^{18}O$ and temperature records developed from foraminiferal geochemistry. *Paleoceanography*, *31*, 1409–1422. https://doi.org/10.1002/2016PA002970

Thomson, J., Mercone, D., De Lange, G., & Van Santvoort, P. J. (1999). Review of recent advances in the interpretation of eastern Mediterranean sapropel S1 from geochemical evidence. *Marine Geology*, *153*(1–4), 77–89. https://doi.org/10.1016/S0025-3227(98)00089-9

Thorweihe, U., Brinkmann, P. J., Heinl, M. & Sonntag, C. (1990). Hydrological and hydrogeological investigations in the Darfur area, western Sudan, Berliner Geowissenschaftliche Abhandlungen, Reihe A.

Thunell, R. C., & Williams, D. F. (1983). Paleotemperature and paleosalinity history of the estern Mediterranean during the Late Quaternary. *Palaeogeography, Palaeoclimatology, Palaeoecology*, *44*(1–2), 23–39. https://doi.org/10.1016/0031-0182(83)90003-2

Torfstein, A., Goldstein, S. L., & Stein, M. (2018). Enhanced Saharan dust input to the Levant during Heinrich stadials. *Quaternary Science Reviews*, *186*, 142–155. https://doi.org/10.1016/j.quascirev.2018.01.018

Tzedakis, P. C., Frogley, M. R., & Heaton, T. H. E. (2003). Last Interglacial conditions in southern Europe: evidence from Ioannina, northwest Greece. *Global and Planetary Change*, *36*(3), 157–170. https://doi.org/10.1016/S0921-8181(02)00182-0

Vergnaud-Grazzini, C., Ryan, W. B. F., & Bianca Cita, M. (1977). Stable isotopic fractionation, climate change and episodic stagnation in the eastern Mediterranean during the late Quaternary. *Marine Micropaleontology*, *2*, 353–370. https://doi.org/10.1016/0377-8398(77)90017-2

Vörösmarty, C. J., Fekete, B. M., Meybeck, M., & Lammers, R. B. (2000). Global system of rivers: Its role in organizing continental land mass and defining land-to-ocean linkages. *Global Biogeochemical Cycles*, *14*(2), 599–621. https://doi.org/10.1029/1999GB900092

Weldeab, S., Emeis, K.-C., Hemleben, C., Schmiedl, G., & Schulz, H. (2003). Spatial productivity variations during formation of sapropels S5 and S6 in the Mediterranean Sea: Evidence from Ba contents. *Palaeogeography, Palaeoclimatology, Palaeoecology*, *191*(2), 169–190. https://doi.org/10.1016/S0031-0182(02)00711-3

Wu, J., Liu, Z., Stuut, J.-B. W., Zhao, Y., Schirone, A., & de Lange, G. J. (2017). North-African paleodrainage discharges to the central Mediterranean during the last 18,000 years: A multiproxy characterization. *Quaternary Science Reviews*, *163*, 95–113. https://doi.org/10.1016/j.quascirev.2017.03.015

Wulf, S., Hardiman, M. J., Staff, R. A., Koutsodendris, A., Appelt, O., Blockley, S. P. E., et al. (2018). The marine isotope stage 1–5 cryptotephra record of Tenaghi Philippon, Greece: Towards a detailed tephrostratigraphic framework for the Eastern Mediterranean region. *Quaternary Science Reviews*, *186*, 236–262. https://doi.org/10.1016/j.quascirev.2018.03.011

Zhuravleva, A., Bauch, H. A., & Van Nieuwenhove, N. (2017). Last Interglacial (MIS5e) hydrographic shifts linked to meltwater discharges from the East Greenland margin. *Quaternary Science Reviews*, *164*, 95–109. https://doi.org/10.1016/j.quascirev.2017.03.026

References From the Supporting Information

Artale, V., Iudicone, D., Santoleri, R., Rupolo, V., Marullo, S., & D'Ortenzio, F. (2002). Role of surface fluxes in ocean general circulation models using satellite sea surface temperature: Validation of and sensitivity to the forcing frequency of the Mediterranean thermohaline circulation. *Journal of Geophysical Research*, *107*(C8), 3120. https://doi.org/10.1029/2000JC000452

Bryden, H., Candela, J., & Kinder, T. (1994). Exchange through the Strait of Gibraltar. *Progress in Oceanography*, *33*(3), 201–248. https://doi.org/10.1016/0079-6611(94)90028-0

Pierre, C. (1999). The oxygen and carbon isotope distribution in the Mediterranean water masses. *Marine Geology*, *153*(1-4), 41–55. https://doi.org/10.1016/S0025-3227(98)00090-5